



A conservative second order phase field model for simulation of N -phase flows

Shahab Mirjalili*, Ali Mani

Center for Turbulence Research, Stanford University, Stanford, CA 94305, USA



ARTICLE INFO

Keywords:

N -phase flow
Phase field
Diffuse interface
Ternary flow
Conservative Allen–Cahn equation
Multi-component flow

ABSTRACT

We present a novel N -phase extension to the second-order conservative phase field method, first introduced by Chiu and Lin [1]. The proposed N -phase model is in conservative form and is symmetric with respect to the phases while satisfying volume conservation. The model is reduction consistent, meaning that in the absence of M phases, the equations reduce to the equations for an $N - M$ -phase flow. This eliminates the possibility of fictitious phases appearing. For coupling to momentum transport, we extend the two-phase mass-momentum consistent model to N -phase flows. By adopting second-order central spatial schemes, the boundedness properties of the two-phase model are inherited by the N -phase model, and the coupled mass-momentum consistent N -phase flow solver inherits the conservation properties of its two-phase version, resulting in the first N -phase flow method that analytically and discretely conserves mass, momentum and kinetic energy (in the absence of capillary and viscous effects). A novel surface tension model is proposed for modeling surface tension forces in N -phase flows. The phase field model allows for variable interface thicknesses between different phase pairs. This endows the model with the property of attaining correct equilibrium configurations at triple junction points. Specifically, we analytically demonstrate that by using interfacial thicknesses that are inversely proportional with the pairwise surface tension, the coupled system achieves steady state at the correct configuration. Using several canonical and practical numerical tests, we demonstrate the accuracy of the phase field equation, the surface tension model, and the fully coupled N -phase flow solver.

1. Introduction

Flows involving interactions of more than two immiscible phases, known as N -phase flows ($N \geq 3$), are common in many practical environmental and engineering problems. For instance, the Deepwater Horizon oil spill was a three-phase flow involving oil, water, and air [2]. Other applications of significant interest where N -phase flows play an important role include enhanced oil recovery [3,4], fuel cells [5], emulsions [6,7], microfluidics [8], and additive manufacturing [9]. Accurate modeling of such flows is therefore highly sought. The most popular approaches for simulating two-phase flows are the Volume-of-Fluid (VOF), Level-Set, and phase field methods. All of these approaches belong to the category of one-fluid models, wherein a single momentum transport equation is solved coupled to a phase transport equation [10–12]. While VOF and Level-Set are sharp-interface models, phase field models represent the transition between two phases using a diffuse interface. For sharp-interface models, many extensions for simulating

* Corresponding author.

E-mail addresses: ssmirjal@stanford.edu (S. Mirjalili), alimani@stanford.edu (A. Mani).

ternary ($N = 3$) or N -phase flows have been proposed within the literature (see [13–16] for VOF and [17–20] for Level Set). Several N -phase flow methods have also been proposed based on solving phase field equations in the framework of Eulerian one-fluid models [21–30], and lattice Boltzmann methods [31–39].

Phase field methods have become a popular alternative to VOF and Level-Set methods for capturing the advection of interfaces in two-phase flows [40,12]. This is primarily owing to their simplicity, parallel efficiency, regularity (smoothness of fields), mass conservation properties, and overall favorable cost versus accuracy tradeoff [41]. The majority of efforts on simulating immiscible two-phase flows with no phase change use the Cahn–Hilliard equation which is a fourth-order partial differential equation (PDE) in conservative form, admitting energy laws that result in robustness and stability. Solving a fourth-order partial differential equation is cumbersome. Additionally, on the PDE level, the Cahn–Hilliard phase field model suffers from inherent problems such as unphysical coarsening of flow features, artificial shrinkage (mass leakage) of drops and bubbles, and lack of bounded solutions for the phase field variable [42,43]. Tackling these is an active area of research and plenty of recent progress has been made towards overcoming these shortcomings [43–46]. Regardless, such difficulties have prompted the search for conservative second-order PDE models based on the Allen–Cahn equation. In its original form, the Allen–Cahn equation results in curvature driven flow, making it unsuitable for simulation of immiscible, incompressible two-phase flows with no phase change. There have been considerable efforts in using space and time dependent Lagrange multipliers to enforce mass conservation [47–51]. As an alternative, locally-conservative approach, by manipulating the Allen–Cahn equation, the second-order conservative phase field model, also known as the conservative Allen–Cahn equation, was derived by [1], which is given by

$$\frac{\partial \phi}{\partial t} + \nabla \cdot (\vec{u}\phi) = \nabla \cdot \gamma[\epsilon \nabla \phi - \phi(1-\phi)\vec{n}], \quad (1)$$

where ϕ is the phase field variable, with $\phi = 0$ and $\phi = 1$ representing the pure phases, $\vec{n} = \nabla \phi / |\nabla \phi|$ is the normal vector, ϵ is the parameter governing the interface thickness, and γ is the other free parameter controlling the strength of the right hand side (RHS) terms. We presented a bounded discretization approach for this equation in [52], and provided a guideline for the choice of ϵ and γ . Later, we presented a model for consistent, kinetic-energy conserving momentum transport for two-phase flow simulations with this phase field model in [53]. Most recently, in [54], we assessed various surface tension models in the context of two-phase simulations with second-order conservative phase field models such as Eq. (1). We showed that compared to the traditional continuum surface force (CSF) model, an energy-based surface tension model and a localized continuum surface force (LCSF) model can reduce spurious currents and achieve higher accuracy.

There have been a few attempts to extend Eq. (1) to ternary or N -phase flows. The equations proposed by [28] and [36] suffer from a lack of mass conservation. In [33], Eq. (1) was extended to ternary fluids. Their model is in conservative form, is symmetric with respect to the phases, and reduces to the two-phase equations in the absence of one of the phases (reduction consistency). However, as is demonstrated by our numerical tests in Section 5.1.1, our finite-difference implementation of their equations in our framework results in nonphysical creation of three-phase zones, in addition to not yielding bounded solutions for the phase field variables. [55] proposed an N -phase extension to Eq. (1) which was in conservative form but was not reduction-consistent. The same authors followed up with a reduction-consistent N -phase flow model in [35]. This was achieved by introducing a Lagrange multiplier to the equations, similar to [33]. The form of the Lagrange multiplier in their work is different from that of [33]. Nevertheless, in a similar way, as shown in Section 5.1.1, our finite-difference implementation of their phase field equation also suffers from a lack of bounded solutions and the creation of artificial three-phase zones. During the review process, it was brought to our attention that a comparative study of the model presented in this work versus the model of [35] is performed in [56]. Using a consistent and conservative Lattice Boltzmann method and an energy-based surface tension force for both models, the authors performed a detailed comparison of the accuracy and stability of the two models. They found that the model of [35] resulted in artificial effects, inaccuracies, and unstable simulations for realistic N -phase flows. On the other hand, simulations using our model were robust and accurate for all test cases.

In this work, we propose a novel N -phase extension to Eq. (1) that is in conservative form, reduction consistent, symmetric with respect to the phases (same equation holds for all N phases), total volume conserving, and inherits the boundedness properties of the two-phase model introduced in [52]. In its general form, the model allows for different interfacial thickness parameters, ϵ_{pq} , between different phase pairs ($1 \leq p, q \leq N$). The model takes advantage of pairwise volume fractions and normal vectors, $\nabla \phi_{pq}$ and \vec{n}_{pq} , defined between all phase pairs $1 \leq p, q \leq N$ —a concept that, to the best of our knowledge, has not been used prior to our work. This allows us to achieve all the above desirable properties without invoking any Lagrange multipliers, in contrast to the state-of-the-art N -phase flow extensions to Eq. (1) [33,35]. For coupling to momentum transport, we extend the two-phase mass-momentum consistent model introduced in [53] to N -phase flows. Since we use the same second-order nondissipative spatial schemes for N -phase flows, the resulting N -phase flow solver is not only mass-momentum consistent, but also inherits the conservation properties of its two-phase version, resulting in the first N -phase flow solver that analytically and discretely conserves mass, momentum and kinetic energy in the absence of capillary and viscous effects. A novel surface tension model is proposed for surface tension forces, leveraging the pairwise volume fractions (ϕ_{pq}), normal vectors (\vec{n}_{pq}) and surface tension coefficients (σ_{pq}). With this surface tension model and with the choice of ϵ_{pq} proportional to $1/\sigma_{pq}$, the fully-coupled N -phase flow model has the analytical property of achieving the correct equilibrium configuration of triple junction points (points where the three components coexist). Our numerical results demonstrate that in addition to the aforementioned desirable properties, our N -phase flow method accurately captures the physics of N -phase flows for practical problems.

In the following, we first introduce the N -phase model in Section 2 and prove its aforementioned properties. In Section 3, we present the numerical discretization schemes that we have employed and then prove why our method is bounded in Section 4. In

Section 5, we present results from numerical tests showing the accuracy of phase field advection, surface tension force calculation, and fully coupled two-dimensional (2D) and three-dimensional (3D) three-phase simulations. Finally, we conclude this work in Section 6.

2. N -phase model

In a flow with D_f spatial dimensions, two-phase interfaces are manifolds with $D_f - 1$ dimensions, and triple-phase zones where three phases interact have $D_f - 2$ dimensions. As such, in a three-dimensional setting, two-phase interfaces are planes, while three phases interact in the vicinity of triple-phase junction lines. Indeed, most interfaces in N -phase systems are between two phases, and it is therefore imperative for the N -phase model to locally converge to the two-phase model given by Eq. (1) in zones where essentially only two phases are present (i.e. away from triple-phase junctions). From this perspective, we propose the following second-order conservative PDE as an N -phase extension to Eq. (1),

$$\frac{\partial \phi_p}{\partial t} + \nabla \cdot (\vec{u} \phi_p) = \gamma \nabla \cdot [\epsilon \nabla \phi_p - \sum_{q \neq p} \frac{\phi_p \phi_q}{(\epsilon_{pq}/\epsilon)} \vec{n}_{pq}] \quad \text{for } 1 \leq p \leq N, \quad (2)$$

where ϵ_{pq} is the parameter representing the pairwise interfacial thickness between phases p and q . As we will explain, one needs to solve Eq. (2) for only $N - 1$ of the phases and use volume conservation, $\sum_p \phi_p = 1$, to compute the remaining phase field variable. The pairwise normal vector is defined as

$$\vec{n}_{pq} = \frac{\nabla \phi_{pq}}{|\nabla \phi_{pq}|} \quad \text{for } q \neq p, \quad (3)$$

computed based on the pairwise volume fraction,

$$\phi_{pq} = \frac{\phi_p}{\phi_p + \phi_q} \quad \text{for } q \neq p. \quad (4)$$

Let us first show that the model satisfies volume conservation, $\sum_p \phi_p = 1$. From Eq. (4), it is clear that $\phi_{qp} = 1 - \phi_{pq}$, as a result of which, $\nabla \phi_{qp} = -\nabla \phi_{pq}$ and $\vec{n}_{qp} = -\vec{n}_{pq}$. Thus, by summing Eq. (2) for all N phases, the nonlinear terms all cancel out, giving

$$\frac{\partial}{\partial t} \sum_p \phi_p = \gamma \epsilon \nabla^2 (\sum_p \phi_p). \quad (5)$$

Hence, assuming $\sum_p \phi_p = 1$ everywhere at $t = 0$, Eq. (2) preserves this property on the continuous and discrete level. In other words, time-integrating Eq. (2) for all N phases is equivalent to solving for only $N - 1$ phases and using $\sum_p \phi_p = 1$ to compute the remaining phase field variable. We adopt the latter choice in order to reduce the number of stored variables and time-integrated PDE's (reducing memory and computational costs). This equivalence coupled with the fact that Eq. (2) has the same form for all phases is why the solutions do not depend on the choice of the $N - 1$ phases for which time integration is performed, which is why the model is declared to be symmetric with respect to the N phases.

Next, let us show that the model is reduction consistent, meaning that in the absence of M phases, the equations reduce to the equations for an $N - M$ phase flow (for $M < N$). Consider $A = \{a_1, a_2, \dots, a_M\}$ to be the set of phase indices that are absent; $\phi_{a_i} = 0$ everywhere for $1 \leq i \leq M$. Firstly, Eq. (2) results in a zero right-hand-side value for all $p \in A$, meaning that $\phi_p = 0$ is maintained and these M phases will not be artificially created. Furthermore, in the remaining $N - M$ equations in Eq. (2), $p \notin A$, all the nonlinear terms involving products with absent phases are zero, $\phi_p \phi_q \vec{n}_{pq} = 0$, because $\phi_q = 0$ for $q \in A$. As such, the remaining $N - M$ equations for the transport of ϕ_p values, where $p \in A$, are identical to the set of equations that govern the corresponding $N - M$ phase flow, and our model is reduction consistent. As an example, in the case of a ternary flow system, in the absence of phase 3 at $t = 0$, we have $\phi_3(\vec{x}, t = 0) = 0$ and $\phi_1(\vec{x}, t = 0) = 1 - \phi_2(\vec{x}, t = 0)$. The transport equation for ϕ_3 becomes $\partial \phi_3 / \partial t = 0$; therefore $\phi_3(\vec{x}, t) = 0$ and owing to volume conservation we have $\phi_1(\vec{x}, t) = 1 - \phi_2(\vec{x}, t)$. Plugging this into the remaining two equations in Eq. (2), it is easy to confirm that the two equations are identical to the two-phase conservative phase field equation given by Eq. (1), whereby ϕ could be chosen as either ϕ_1 or ϕ_2 .

Using the same discretization strategy as in the two-phase flow methods presented in [52,53], the N -phase extension given by Eq. (2) inherits the boundedness property, as proven in Section 4. More explicitly, defining the interfacial thickness parameter ϵ such that $\epsilon \leq \epsilon_{pq}$ for $1 \leq p, q \leq N$, the same criteria for choosing ϵ and γ guarantees positivity of ϕ in Eq. (1) and all ϕ_p variables in Eq. (2) (without incurring any additional time step restriction). This results in $0 \leq \phi_p \leq 1$ for all phases ($1 \leq p \leq N$) at all times, which is crucial in terms of robustness and realizability of the solutions.

We adopt a one-fluid model, which means that the phase field equations for the N phases (Eq. (2)) are coupled to a single equation for momentum transport. This momentum transport equation is in conservative form and includes the correction for mass-momentum consistency [30,53],

$$\frac{\partial(\rho \vec{u})}{\partial t} + \nabla \cdot [(\rho \vec{u} - \vec{S}) \otimes \vec{u}] = -\nabla P + \nabla \cdot [\mu(\nabla \vec{u} + \nabla^T \vec{u})] + \vec{F}_{\text{ST}}. \quad (6)$$

In Eq. (6), P is the pressure field, ρ is the density field computed via

$$\rho = \sum_p \rho_p \phi_p, \quad (7)$$

μ is the fluid viscosity, computed via

$$\mu = \sum_p \mu_p \phi_p, \quad (8)$$

and \vec{S} is the mass-momentum consistency correction flux, given by

$$\vec{S} = \sum_p \rho_p \vec{R}_p, \quad (9)$$

where \vec{R}_p is the term inside the divergence on the RHS of Eq. (2), $\vec{R}_p = \gamma [\epsilon \nabla \phi_p - \sum_{q \neq p} \frac{\phi_p \phi_q}{(\epsilon_{pq}/\epsilon)} \vec{n}_{pq}]$ for phase p . Note that in Eq. (6), by solving for the momentum of the N -phase fluid in conservative form, and by accounting for the artificial mass flux by including \vec{S} , the kinetic energy of the system is conserved in the absence of surface tension and viscous forces. Since we use second-order central differences for spatial discretization, kinetic energy can also be shown to be conserved discretely. The proof of this property was presented in [53] for two-phase flows, and the extension to N -phase flows is trivial. It is worth remarking that the mass-momentum consistency is critical and necessary for accurate and robust simulations of high-density ratio multi-phase flows.

The surface tension force in Eq. (6), \vec{F}_{ST} is modelled by

$$\vec{F}_{ST} = \sum_{p < q} 6\sigma_{pq} \kappa_{pq} \phi_p \phi_q \nabla \phi_{pq}, \quad (10)$$

where σ_{pq} is the pairwise surface tension coefficient between phases p and q and κ_{pq} is the pairwise curvature computed using the pairwise normal vectors,

$$\kappa_{pq} = -\nabla \cdot \vec{n}_{pq} \quad \text{for } q \neq p. \quad (11)$$

Note that the surface tension force in Eq. (10) is an N -phase extension of the LCSF model recently introduced for two-phase flows in [54]. To explain, in the two-phase case, the model is $\vec{F}_{ST} = 6\sigma_{12} \kappa_{12} \phi_1 \phi_2 \nabla \phi_{12}$, which is equivalent to the traditional CSF model localized by the kernel of $6\phi_1 \phi_2$. We have shown that for two-phase simulations using second-order phase field models, this localization results in more accurate results compared to traditional CSF [54]. We adopt this surface tension model because of this improved accuracy and because it results in point-wise zero surface tension forces for equilibrium triple junction points and flat interfaces (see Section 2.1). As shown in our previous work, [54], the LCSF model and the energy-based model used in [31,38,55,35,30] are equivalent for two-phase interfaces in equilibrium. As such, the forces should converge to the same values in two-phase regions where the interfaces are in equilibrium. Generally, however, the N -phase extensions of the energy-based surface tension model (used in [31,38,55,35,30]) and the model introduced in Eq. (10) are not equivalent. In any case, recent work by [56] uses the energy-based surface tension approach in combination with our N -phase model (Eq. (25)), and demonstrate accurate and robust results similar to the results we present in Section 5 of this work.

We next examine the equilibrium solution to our proposed N -phase model in Section 2.1. In particular, we show that the phase field equation with variable interfacial thickness parameters (Eq. (2)) coupled to Eqs. (6) and (10) results in the correct force balance at triple junction points if the interfacial thickness parameters are chosen to scale with the inverse of the surface tension coefficients.

2.1. Equilibrium solution

At equilibrium, the two-phase model in Eq. (1) attains a hyperbolic tangent profile given by $\phi = [1 + \tanh(\psi/2\epsilon)]/2$, where ψ is the signed distance function from the $\phi = 0.5$ contour line [1,52]. This is in accordance with the classical theory of capillary interfaces [57–59] and intuitively reasonable. Even for the case of $N = 3$, however, the expected analytical equilibrium solution for ϕ_1 , ϕ_2 , and ϕ_3 is not obvious for a three phase system with diffuse interfaces, regardless of the choice of PDEs. In what follows, we first introduce an expected analytical equilibrium solution. After gaining intuition about it, we demonstrate that our proposed phase field model indeed honors this expected field as its equilibrium solution.

N -phase systems are well-defined in the sharp-interface limit, as shown schematically for a triple junction point in Fig. 1(a). However, it is not trivial to imagine an equilibrium triple junction zone for diffuse interfaces. Let us define the scalar field of ψ_{pq} as the signed distance function from the $\phi_{pq} = 0.5$ contour line, defined to increase from phase q to phase p . Then, for an N -phase system with diffuse interfaces, we expect the equilibrium solution to satisfy

$$\phi_{pq} = \frac{1}{2} [1 + \tanh(\frac{\psi_{pq}}{2\epsilon_{pq}})] = \frac{1}{1 + \exp(\frac{-\psi_{pq}}{\epsilon_{pq}})} \quad \text{for } q \neq p. \quad (12)$$

This is because this equation automatically reduces to the two-phase equilibrium profile in two-phase regions of the system. Using the definition of the pairwise volume fractions (Eq. (4)), algebraic manipulation of Eq. (12) results in

$$\frac{\phi_p}{\phi_q} = \frac{\phi_{pq}}{\phi_{qp}} = \exp(\frac{\psi_{pq}}{\epsilon_{pq}}) \quad \text{for } q \neq p. \quad (13)$$

This relationship between different phase pairs coupled to conservation of total volume specifies the phase field variables,

$$\phi_p = \frac{1}{1 + \sum_{q \neq p} \exp(-\frac{\psi_{pq}}{\epsilon_{pq}})} \quad \text{for } 1 \leq p \leq N. \quad (14)$$

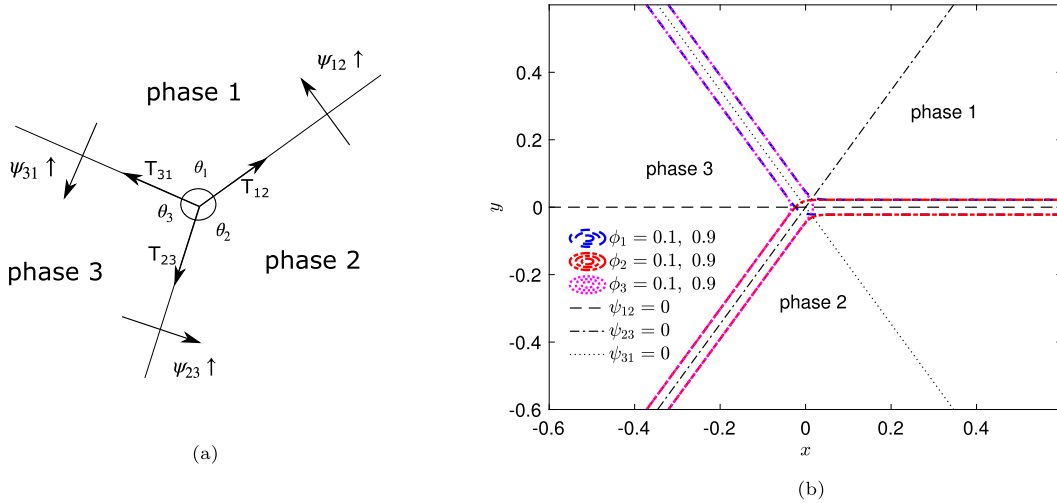


Fig. 1. (a) A schematic of a triple junction zone in the physical sharp-interface limit, (b) analytical solution for a triple junction solution satisfying Eq. (13).

Equation (13) constrains the choice of the pairwise distance functions (ψ_{pq}) and interfacial thickness parameters (ϵ_{pq}). Consider the triple junction zone shown schematically in Fig. 1 (a). For the two-phase regions' solutions given by Eq. (13) to extend to the triple junctions, requires

$$\left(\frac{\phi_1}{\phi_2}\right)\left(\frac{\phi_2}{\phi_3}\right)\left(\frac{\phi_3}{\phi_1}\right) = \exp\left(\frac{\psi_{12}}{\epsilon_{12}} + \frac{\psi_{23}}{\epsilon_{23}} + \frac{\psi_{31}}{\epsilon_{31}}\right) = 1, \quad (15)$$

hence, requiring

$$\frac{\psi_{12}}{\epsilon_{12}} + \frac{\psi_{23}}{\epsilon_{23}} + \frac{\psi_{31}}{\epsilon_{31}} = 0 \quad (16)$$

to hold everywhere in the domain. If we take the gradient of Eq. (16), we obtain

$$\frac{1}{\epsilon_{12}} \nabla \psi_{12} + \frac{1}{\epsilon_{23}} \nabla \psi_{23} + \frac{1}{\epsilon_{31}} \nabla \psi_{31} = 0. \quad (17)$$

Note that since ψ_{pq} are signed distance functions, these gradients are unit vectors normal to the sharp interfaces, pointing from phase q to p (see Fig. 1). As such, Eq. (17) gives a relation between three vectors of size $1/\epsilon_{pq}$ forming a triangle with angles specified by the triple point angles (θ_i for $i = 1, 2, 3$). Based on the law of sines, the equilibrium solution defined in Eq. (12) can only hold at the triple junction zone if the interfacial thickness parameters and triple point angles satisfy

$$\epsilon_{12} \sin \theta_3 = \epsilon_{23} \sin \theta_1 = \epsilon_{31} \sin \theta_2. \quad (18)$$

Therefore, in order for the expected equilibrium solution (Eqs. (12)-(14)) to be valid everywhere, the interfacial thickness parameters must be selected based on the desired triple point contact angles. As a pedagogical example, consider a triple junction point at $(x, y) = (0, 0)$ in a two-dimensional setting. We define the three signed distance functions to be given by $\psi_{12} = y$, $\psi_{23} = \sqrt{3}x/2 - y/2$, and $\psi_{31} = -\sqrt{3}x/2 - y/2$, corresponding to $\theta_i = 120^\circ$ for all three phases. From Eq. (18) we know that the interfacial thickness parameters must be equal among all phase pairs. Selecting the interfacial thicknesses to all be 0.01, we can find ϕ_1 , ϕ_2 , and ϕ_3 analytically using Eq. (14). Contour lines of the phase field variables and the signed distance functions for this scenario are shown in Fig. 1(b). It is clear that the 360° around the triple junction point are divided to three 120° angles for each phase with equal interfacial thicknesses between all three pairs.

Now, we show that the solution given by Eq. (12) is indeed an equilibrium solution to Eq. (2), even at zones where multiple phases are interacting, such as triple junctions. As we know from the two-phase scenario, Eq. (12) satisfies

$$\nabla \phi_{pq} - \frac{\phi_{pq}(1 - \phi_{pq})}{\epsilon_{pq}} \vec{n}_{pq} = 0 \quad \text{for } q \neq p, \quad (19)$$

for each pair of p and q . Using Eq. (4) to expand Eq. (19) along with some algebra we obtain

$$\phi_q \nabla \phi_p - \phi_p \nabla \phi_q - \frac{\phi_p \phi_q}{\epsilon_{pq}} \vec{n}_{pq} = 0 \quad \text{for } q \neq p. \quad (20)$$

Summing the $N - 1$ equations in Eq. (20) for $q \neq p$, multiplying by $\gamma \epsilon$, and using total volume conservation, $\sum_p \phi_p = 1$,

$$\vec{R}_p = \gamma(\epsilon \nabla \phi_p - \sum_{q \neq p} \frac{\phi_p \phi_q}{(\epsilon_{pq}/\epsilon)} \vec{n}_{pq}) = 0 \quad \text{for } 1 \leq p \leq N, \quad (21)$$

i.e., the RHS term in Eq. (2) is zero for all phases and thus, the solution defined by Eqs. (12)-(14) is indeed an equilibrium solution to Eq. (2) everywhere.

So far we have shown that with the appropriate selection of the interfacial thickness parameters, the proposed expected analytical solution is an equilibrium solution to the phase field equations. Now let us turn to the momentum equation. For the coupled system to achieve equilibrium, we require momentum equilibrium in addition to phase field equilibrium. The mechanical balance of surface tension forces at the triple junction point, also known as Neumann's vector relation [60], gives

$$\sigma_{12}\vec{T}_{12} + \sigma_{23}\vec{T}_{23} + \sigma_{31}\vec{T}_{31} = 0, \quad (22)$$

where T_{pq} are unit vectors aligned with the interfaces as shown schematically in Fig. 1(a). It is in fact this balance that determines the triple point angles (θ_i) in real systems, $\sigma_{12}/\sin \theta_3 = \sigma_{23}/\sin \theta_1 = \sigma_{31}/\sin \theta_2$. Since T_{pq} is equal to $\nabla \psi_{pq}$ rotated 90° in the clockwise direction, we have

$$\sigma_{12}\nabla \psi_{12} + \sigma_{23}\nabla \psi_{23} + \sigma_{31}\nabla \psi_{31} = 0. \quad (23)$$

Comparing Eqs. (17) and (23), and noting that $\nabla \psi_{pq}$ are unit vectors, the two vector relations simultaneously hold if and only if

$$\epsilon_{12}\sigma_{12} = \epsilon_{23}\sigma_{23} = \epsilon_{31}\sigma_{31}. \quad (24)$$

In other words, for consistency between the expected phase field equilibrium solution and mechanical balance of surface tension forces at triple junction zones, the interfacial thickness parameters (ϵ_{pq}) must be chosen consistently with respect to the surface tension coefficients, (σ_{pq}) using Eq. (24). Crucially, the expected analytical solution given by Eqs. (12)-(14) also satisfies momentum equilibrium for our N -phase momentum equation (Eq. (6)). Specifically, for a stationary system ($\vec{u} = 0$), the inertial and viscous terms are zero. In the vicinity of a triple junction, the ψ_{pq} fields are distance functions from straight lines and are thus affine functions in space, resulting in constant \vec{n}_{pq} vectors. This results in zero pairwise curvature fields $\kappa_{pq} = 0$, and surface tension forces that are point-wise zero according to Eq. (11). The pressure field is therefore uniform around the triple junction, and the expected analytical solution satisfies momentum equilibrium. In summary, by choosing the interface thickness parameters according to Eq. (24), our fully coupled N -phase model—both phase field and Navier–Stokes equations—satisfies a well-defined expected equilibrium solution for triple junction points.

2.2. Selection of interfacial thickness parameters

For the case of equal interfacial thickness parameters between all phase pairs, $\epsilon_{pq} = \epsilon$, Eq. (2) reduces to

$$\frac{\partial \phi_p}{\partial t} + \nabla \cdot (\vec{u} \phi_p) = \gamma \nabla \cdot (\epsilon \nabla \phi_p - \sum_{q \neq p} \phi_p \phi_q \vec{n}_{pq}) \quad \text{for } 1 \leq p \leq N. \quad (25)$$

It is commonly known in the context of phase field methods that the accuracy of capturing the interface evolution and dynamics of two-phase flows increase as one decreases the interfacial thickness parameter. Moreover, in order to resolve the interface and achieve bounded solutions (i.e., avoid dispersion errors), as one decreases the interface thickness, the mesh sizing should be decreased as well [52]. In the two-phase case, for a given mesh, in order to achieve maximum accuracy, one desires to use a small $\epsilon/\Delta x$ value while obeying the boundedness criteria established in [52]. As shown in Section 4, the same boundedness criterion holds for the N -phase model. As such, in practice, we often solve Eq. (25) because most interfacial regions are indeed two-phase regions. Doing so, the model forgoes the analytical property at triple junction points described in Section 2.1 to obtain higher accuracy everywhere else (unless surface tensions are all equal). Utilization of variable interfacial thickness parameters can be particularly useful when we are most interested in predicting the equilibrium state of triple junctions accurately. In summary, for a given mesh, there is a tradeoff between capturing triple junctions accurately while losing accuracy in two-phase regions by using variable interfacial thickness parameters (Eq. (24)) versus minimizing interfacial thicknesses ($\epsilon_{pq} = \epsilon$) to gain accuracy in all interfacial regions except for triple junction zones. We demonstrate this tradeoff using our numerical tests in Sections 5.1, 5.3, and 5.5.

3. Computational approach

We use a fourth-order Runge-Kutta (RK4) explicit scheme for time integration. Other explicit time integration schemes such as RK2 can be used without significant loss of accuracy, since the spatial discretization errors are dominant (see Section 5.1). Nevertheless, we use RK4 mainly due to its large stability region, which is particularly advantageous for problems with low or zero viscosity [61]. At each time step, $N - 1$ phase field equations, Eq. (2) (or (25) for constant interfacial thickness of ϵ) are time integrated to update $N - 1$ phase field variables, along with volume conservation for the N 'th phase field variable. These equations are coupled to the consistent momentum transport equation given by Eq. (6), which involves computation of density, viscosity and surface tension forces as a function of the phase field variables via Eqs. (7)-(10). In space, we use a second order central finite difference discretization on a standard staggered Cartesian grid, in which velocity vectors and all fluxes, including the phase field fluxes, are stored on their respective faces, while pressure, density, viscosity, and the phase field variables are stored on cell centers. The numerical schemes

are generally extensions of the two-phase flow version described in detail in [53]. For the reader's convenience, we provide the pseudo-algorithm for our coupled solver in Appendix A.

4. Boundedness

The N -phase computational model presented here inherits the boundedness property of its two-phase predecessor, presented in [52]. In particular, $0 \leq \phi_p \leq 1$ is guaranteed from solving Eq. (2), as long as the interfacial thickness parameter, $\epsilon \leq \epsilon_{pq}$ for $1 \leq p, q \leq N$, is chosen such that

$$\epsilon/\Delta x \geq \frac{\gamma/|\vec{u}|_{\max} + 1}{2\gamma/|\vec{u}|_{\max}}, \quad (26)$$

and the timestep is chosen based on stability, $\Delta t \leq C\Delta x^2/(D_f\gamma\epsilon)$, where C is the diffusive CFL number which depends on the time-integration scheme (e.g., $C = 0.5$ for explicit Euler, and $C = 0.7$ for RK4). The detailed proof of the boundedness property for N -phase flows is beyond the scope of this work. We provide the outline of the proof here. As explained in [52], the most restrictive setting for boundedness is a one-dimensional (1D) flow. The essence of the proof in the two-phase flow case is that for a time-step chosen based on stability, the diffusive terms must overcome the aggregate effect of the sharpening and advective terms to dampen overshoots and undershoots. Let's assume all phase field variables are within bounds at a given time, $0 \leq \phi_p \leq 1$ for $1 \leq p \leq N$. For explicit time-stepping, if the RHS terms for ϕ_p are positive, then ϕ_p will remain positive during time-integration. By comparing the two-phase model given in Eq. (1) and the N -phase model in Eq. (2), while the advective and diffusive terms are identical (continuously and discretely), the magnitude of the sharpening flux for the N -phase model is at most equal to the two-phase case and smaller than 1, which is needed for Eq. (26) to guarantee positivity of the RHS,

$$|\sum_{q \neq p} \frac{\phi_p \phi_q}{(\epsilon_{pq}/\epsilon)} \vec{n}_{pq}| \leq |\sum_{q \neq p} \phi_p \phi_q \vec{n}_{pq}| \leq |\sum_{q \neq p} \phi_p \phi_q| \leq \phi_p(1 - \phi_p) \leq 1, \quad (27)$$

where we have used total volume conservation ($\sum_p \phi_p = 1$), $|\vec{n}_{pq}| \leq 1$, and $\epsilon \leq \epsilon_{pq}$. Since the RHS for all ϕ_p values is positive in Eq. (2), ϕ_p values will remain positive during explicit time-integration. Owing to the total volume conservation, $\sum_p \phi_p = 1$, this requires $\phi_p \leq 1$ for $1 \leq p \leq N$, completing the outline of our boundedness proof for the N -phase system.

5. Numerical tests

In this section, we utilize multiple three-phase test cases in 2D and 3D to assess the accuracy and convergence properties of the proposed N -phase models. We examine three-phase flows for the purpose of validating of our model because a larger number of phases ($N \geq 4$) do not introduce major additional complexities in the continuous or discrete sense. We first test the accuracy and convergence of the phase field equations in 2D shear flow with a given velocity field (known in space and time) in Section 5.1. In this test, the performance of the proposed phase field equation is compared against the state-of-the-art in literature [33,35]. Next, we test the accuracy and convergence of curvature calculation in a 2D setting with no flow in Section 5.2. In Section 5.3, we test the coupled model's ability in capturing the correct equilibrium configurations at triple junction zones in a 2D setting. The 2D floating lens problem is examined in Section 5.4. In Section 5.5, we perform an extensive study of a 2D dynamic problem involving the buoyancy-driven fall and rise of two oil drops in air and water, respectively. Finally, a 3D case of an air bubble rising in stratified layers of water and oil is presented in Section 5.6. All values reported in the numerical results are in non-dimensional form, unless noted otherwise.

5.1. Drops in 2D shear flow

We extend the standard drop in 2D shear test for two-phase interface-capturing schemes to three-phase flows. In a 1×1 domain, at $t = 0$, two drops of diameter $D = 0.3$ of phase 1 and 2 are placed at $(0.75, 0.5)$ and $(0.5, 0.75)$, respectively. The initial configuration is shown in Fig. 2a. The velocity field is given by the stream function,

$$\Psi(x, t) = \frac{1}{\pi} \sin^2(\pi x) \sin^2(\pi y) \cos\left(\frac{\pi t}{T}\right), \quad (28)$$

where the period of the imposed velocity field is $T = 4$. Due to the periodic nature of the velocity, this test case has an exact solution at $t = T$, which is given by the initial conditions, or in other words, $\phi_{exact,p}(t = T) = \phi_p(t = 0)$ for $p = 1, 2, 3$. Using equal interfacial thicknesses, $\epsilon_{12} = \epsilon_{23} = \epsilon_{31} = \epsilon$, we perform convergence studies by increasing the mesh resolution while keeping $\epsilon/\Delta x = 0.7$ and $\gamma/|\vec{u}|_{\max} = 2.5$ fixed. A fixed time step of $\Delta t = \Delta x/8$ is used for time integration. Mesh convergence of the results at $t = T/2$ and $t = T$ are shown in Figs. 2b and 2c respectively. These plots demonstrate that the two drops do not interact in this problem and the solutions to each drop match the solutions in the classical two-phase case with a single drop [52], albeit rotated 90° with respect to one another. Essentially, because of the rotational symmetry of the problem, the evolution of the drop of phase 2 is identical to the phase 1 drop, except that it is rotated 90° in the counter-clockwise direction. We observe that at $t = T/2$, both drops are stretched by the velocity field, resulting in the appearance of artificial drops at low resolutions, which are eliminated as we increase the resolution. At $t = T$, we observe that as the mesh is refined, both drops converge to the analytical solution, which is the solution at $t = 0$. Fig. 2d shows the result of a 128×128 single phase calculation at $t = T/2$, where the only thing that has changed is that

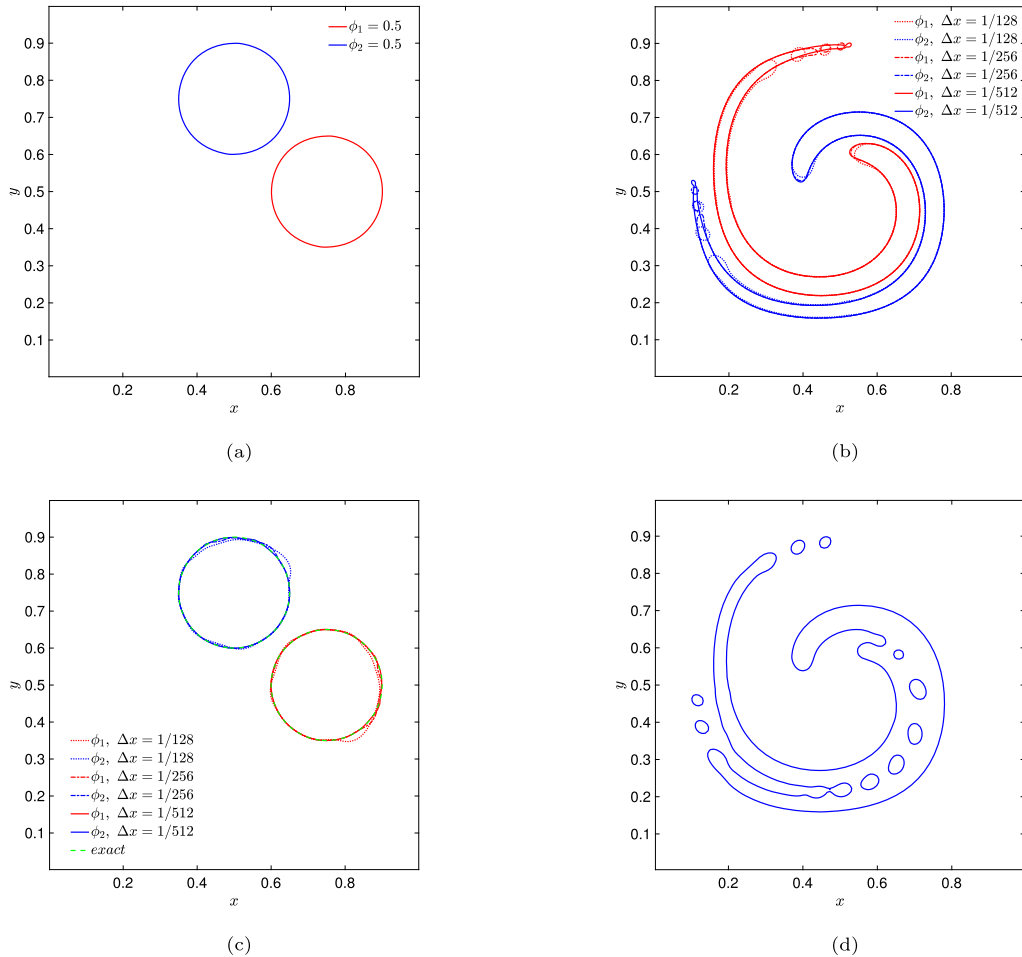


Fig. 2. (a) Initial configuration for the drops in 2D shear flow, (b) contour lines of $\phi_1 = 0.5$ and $\phi_2 = 0.5$ at $t = T/2$, plotted in red and blue respectively, for various resolution simulations, (c) contour lines of $\phi_1 = 0.5$ and $\phi_2 = 0.5$ at $t = T$, plotted in red and blue respectively, for various resolution simulations, compared to the exact solution, (d) the 0.5 contour line for the phase field variable at $t = T/2$, for a two-phase simulation initialized with two drops of the same phase on a 128×128 grid, highlighting the coalescence that is avoided by the 3-phase simulations (shown in panel (b)). (For interpretation of the colors in the figure(s), the reader is referred to the web version of this article.)

the two drops are of the same phase. In this case, since the drops are of the same phase, they coalesce at this coarse resolution. On the other hand, it is clear that as opposed to the single-phase scenario, the N -phase model appropriately prevents coalescence at all resolutions.

A more quantitative measure of accuracy is to compare the solution field for ϕ_p ($p = 1, 2, 3$) at $t = T$ against the initial fields at $t = 0$. We define the error in the solution of ϕ_p as

$$E_{shape,p} = \sum_{i=1}^{N_x} \sum_{j=1}^{N_y} |\phi_p(i,j,t=T) - \phi_p(i,j,t=0)| \Delta x \Delta y. \quad (29)$$

In Fig. 3, the error is plotted as a function of number of mesh points across drop diameter (i.e., resolution). First of all, the shape error for both phase 1 and phase 2 converges with second-order accuracy. Second, using RK2 time stepping does not affect the accuracy of the model for this test because of the dominance of the spatial discretization errors. However, despite being more expensive, RK4 is used for all tests (including the simulations using the phase field models of [33,35]) due to its larger stability region [61].

5.1.1. Comparison against state-of-the-art models

After implementing the ternary phase field model proposed by [33] and the N -phase model by [35] within our framework (with the same computational approach and finite-difference discretization schemes described in Section 3), we compare their accuracy and robustness on this test case against our proposed model. Both of these models are chosen for comparison here as they are the only models within the literature that have extended Eq. (1) to $N \geq 3$, while achieving volume conservation, symmetry, and reduction

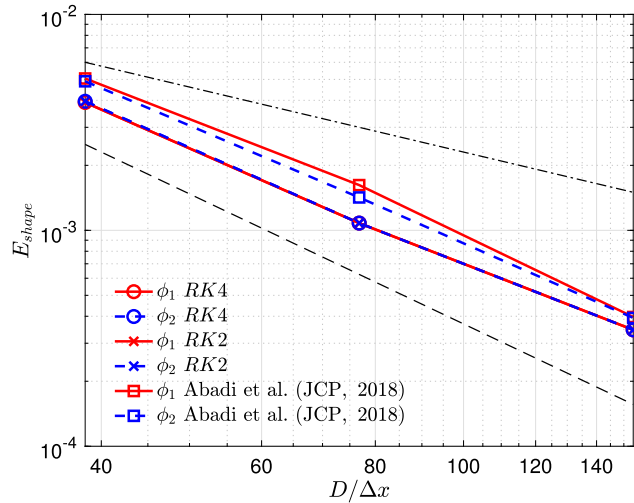


Fig. 3. Shape error for 2D drops in shear flow simulations using the present model with RK4 and RK2 time integration plotted as a function of resolution for phase 1 and 2 in red and blue respectively, compared against simulations performed with the model of Abadi et al. [33]. Dash-dotted and dashed lines represent first and second order convergence rates, respectively.

Table 1

Boundedness of the present model and the models of Abadi et al. [33] and Zheng et al. [35] for multiple resolution simulations of drops in 2D shear flow, compared at $t = T/2$ and $t = T$. In the table, N/A refers to simulations that have become unstable prior to that time.

Model	128 × 128	256 × 256	512 × 512
Abadi et al. [33], $t = T/2$	$-3.40 \times 10^{-3} \leq \phi_1 \leq 1 - 1.47 \times 10^{-3}$	$-3.20 \times 10^{-3} \leq \phi_1 \leq 1 - 1.79 \times 10^{-6}$	$-1.68 \times 10^{-4} \leq \phi_1 \leq 1 + 2.54 \times 10^{-7}$
Abadi et al. [33], $t = T$	$-1.98 \times 10^{-4} \leq \phi_1 \leq 1 + 1.09 \times 10^{-4}$	$-2.37 \times 10^{-4} \leq \phi_1 \leq 1 + 1.20 \times 10^{-5}$	$-3.16 \times 10^{-4} \leq \phi_1 \leq 1 + 2.33 \times 10^{-6}$
Zheng et al. [35], $t = T/2$	$-9.16 \times 10^{-4} \leq \phi_1 \leq 1 + 5.22 \times 10^{-4}$	$-5.27 \times 10^{-7} \leq \phi_1 \leq 1 - 1.07 \times 10^{-6}$	N/A
Zheng et al. [35], $t = T$	$-8.42 \times 10^{-7} \leq \phi_1 \leq 1 + 4.72 \times 10^{-5}$	N/A	N/A
Present model, $t = T/2$	$6.59 \times 10^{-19} \leq \phi_1 \leq 1 - 2.45 \times 10^{-3}$	$7.87 \times 10^{-20} \leq \phi_1 \leq 1 - 1.77 \times 10^{-6}$	$1.67 \times 10^{-21} \leq \phi_1 \leq 1 - 8.29 \times 10^{-13}$
Present model, $t = T$	$9.55 \times 10^{-19} \leq \phi_1 \leq 1 - 7.99 \times 10^{-13}$	$6.16 \times 10^{-20} \leq \phi_1 \leq 1 - 2.22 \times 10^{-16}$	$8.70 \times 10^{-21} \leq \phi_1 \leq 1 - 1.11 \times 10^{-16}$

consistency.¹ Using the same code, and maintaining all simulation parameters while only changing the phase field PDE, we observe that the two state-of-the-art models suffer from multiple issues.

A significant advantage of our model is its boundedness property. In Table 1, the ranges of ϕ_1 values are given at $t = T/2$ and $t = T$ for various resolution simulations using our model and those of [33] and [35]. We observe that while our solutions yield ϕ_1 values between 0 and 1 (as expected based on Section 4), the other models do not predict bounded values for the phase field variables. In fact, with our numerical discretization and choice of free parameters, we observe that the simulations with the model of [35] are unstable on the 256×256 and 512×512 grids.

Shifting our focus to accuracy, Fig. 3 shows that while both our model and the model of [32] converge with second-order accuracy, the former has smaller errors for all resolutions. The results from the model by [35] are excluded from this figure due to unstable simulations at the two higher resolutions. More critically, when inspecting the solution fields, especially at lower resolutions we observe the nonphysical creation of three-phase zones by the models from [33] and [35]. In Fig. 4, we plot $\phi_2 - \phi_1$ at $t = T/2$ from simulations performed on 128×128 (left panels) and 256×256 (right panels) grids using our model (top panels) and the models of [33] (middle panels) and [35] (bottom panel). We observe from panels (c)-(f) nonphysical three-phase zones, created by the models of [33] and [35]. Presumably, this can be ascribed to the addition of the Lagrange multipliers by these models, resulting in artificial effects that our model averts. We note that these artificial effects and the lack of boundedness/robustness may be ameliorated by other discretization schemes (e.g., the Lattice Boltzmann schemes used in [33] and [35]) and/or other choices for the simulation parameters. A more extensive comparison of the present model and other N -phase conservative Allen–Cahn models is beyond the scope of this work. As mentioned in Section 1 though, a detailed comparison between our model and that of [35] can be found in [56], confirming the relative accuracy and stability advantages of our model, especially in realistic flows.

Notably, the two stable models (present model and [32]) result in almost identical solution fields for the highest resolution (512×512 grid, shown in Fig. 5). Fig. 6 compares these two models at $t = T$, whereby we can see from panels (b) and (d) that the lower resolution calculations with the model of [33] result in nonphysical remnants of phase 1 close to the drop of phase 2 and vice versa. Once again, the highest resolution cases (panels (e) and (f)) show that both our model and that of [33] converge to the correct solutions.

¹ Note that we use the model from [35] with the value of $q = 1$ in Eq. 8 of that article.

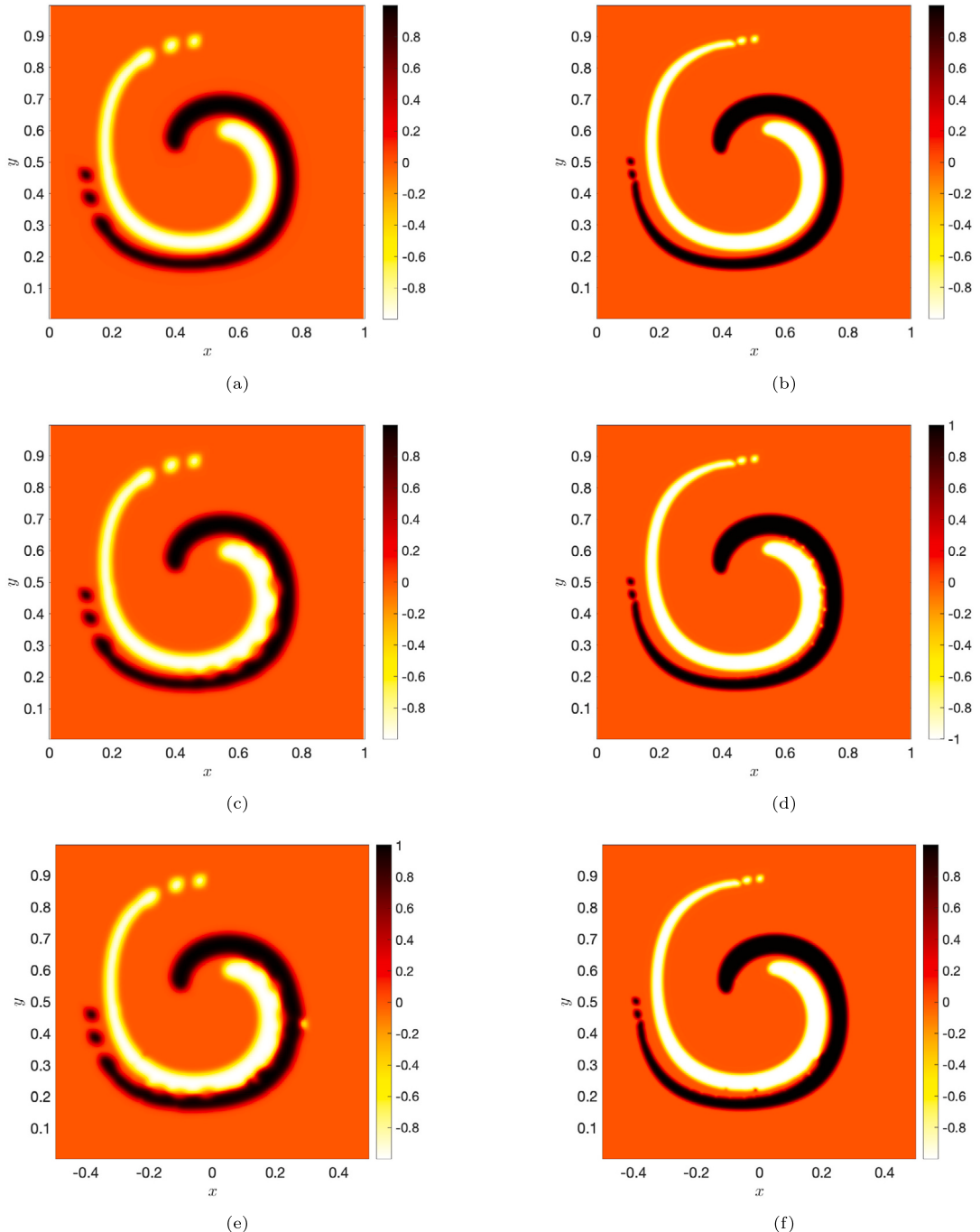


Fig. 4. Plots of $\phi_2 - \phi_1$ at $t = T/2$ for 2D drops in shear flow simulations using (a) present model on a 128×128 grid, (b) present model on a 256×256 grid, (c) Abadi et al. [33] model on a 128×128 grid, (d) Abadi et al. [33] model on a 256×256 grid, (e) Zheng et al. [35] model on a 128×128 grid, (f) Zheng et al. [35] model on a 256×256 grid.

5.1.2. Variable interface thickness

As a demonstration of the dependence of the solutions on the interfacial thickness parameters, here we present results of the solutions from Eq (2) with variable interfacial thickness parameters, $\epsilon_{12} = \epsilon_{23}/4 = \epsilon_{31}/2 = \epsilon$. Fig. 7f depicts the solutions ($\phi_2 - \phi_1$ fields) at $t = T/2$ and $t = T$ for various resolution simulations using our model. Firstly, we observe that the phase 2 drop is more diffused compared to the phase 1 drop, and both are more diffused than the profiles observed at the same resolution with $\epsilon_{12} = \epsilon_{23} = \epsilon_{31} = \epsilon$ in Figs. 4 and 6. Additionally, the thicker interfaces unsurprisingly result in larger errors, manifesting in most severe nonphysical breakup of drops at $t = T/2$, and shape errors at $t = T$, which are worse for the drop of phase 2 than phase 1. As

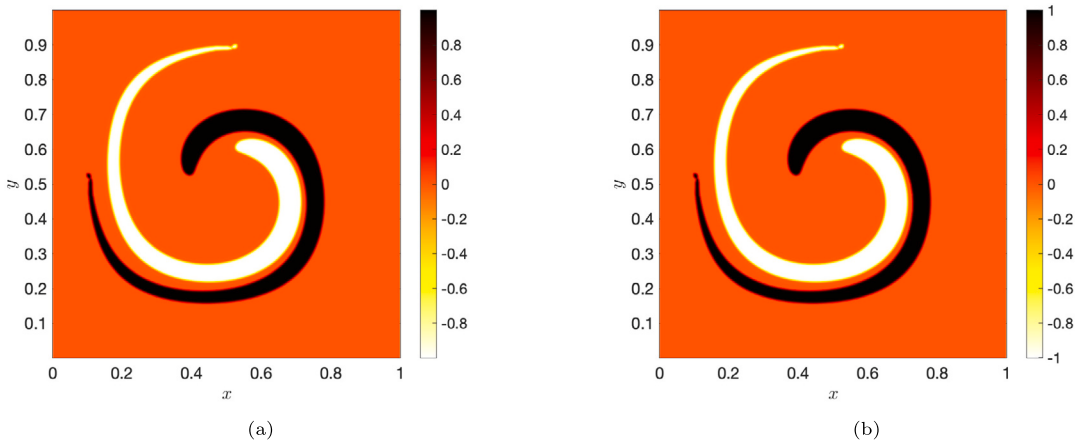


Fig. 5. Plots of $\phi_2 - \phi_1$ at $t = T/2$ for 2D drops in shear flow simulations using (a) present model on a 512×512 grid, (b) Abadi et al. [33] model on a 512×512 grid.

explained in Section 2.2, this is an example of a problem in which predicting the behavior in the triple junction points is not critical, and as a result it is advantageous to use equal interfacial thicknesses, $\epsilon_{pa} = \epsilon = 0.7\Delta x$, to achieve higher accuracy.

5.2. Surface tension accuracy tests

In this test, we assess the accuracy of the surface tension force model in Eq. (10) by examining the pressure jumps across interfaces in static scenarios. We explore three different scenarios using $\epsilon_{12} = \epsilon_{23} = \epsilon_{31} = \epsilon$, and fixed values of $\epsilon/\Delta x = 1$ and $\gamma/|\vec{u}|_{max} = 1$. The domain is 1×1 and periodic boundary conditions are employed on all boundaries. In the first scenario, in a background of phase 3, a drop of phase 1 with radius $R_1 = 0.2$ is placed at $(0.3, 0.5)$, and a drop of phase 2 with radius $R_2 = 0.1$ is placed at $(0.8, 0.5)$ at $t = 0$. The initial velocity field is stationary ($\vec{u} = 0$), and the spatial resolution is 128×128 . The surface tension coefficients are $\sigma_{12} = 0.1$, $\sigma_{23} = 0.3$, and $\sigma_{31} = 0.9$. Based on these values and the Young-Laplace law, the pressure jump in drops of phase 1 and 2 are $P_1 = \sigma_{31}\kappa_{31} = \sigma_{31}/R_1 = 4.5$ and $P_2 = \sigma_{23}\kappa_{23} = \sigma_{23}/R_2 = 3.0$, respectively. Fig. 8(a) depicts simulation results at $t = 0.1$, where the pressure field is plotted in addition to contour lines of $\phi_1 = 0.5$ (blue line) and $\phi_2 = 0.5$ (red line). We observe that the surface tension model in Eq. (10) is yielding the correct pressure jump values. Panel (b) shows the phase field variables and pressure in the cross-section of $y = 0.5$, further confirming the accuracy of the surface tension model. To demonstrate the symmetry of the model, Panel (c) shows the pressure field and phase field contour lines and Panel (d) shows the $y = 0.5$ cross section for the second scenario wherein the phases of the drops have changed. The left drop is of phase 3, while the right drop is of phase 1 and the background is phase 2. Keeping everything else the same, we observe in Panels (c) and (d) the correct pressure jumps of $P_3 = \sigma_{32}\kappa_{32} = \sigma_{32}/R_2 = 1.5$ and $P_1 = \sigma_{12}\kappa_{12} = \sigma_{12}/R_1 = 1.0$ from our numerical results at $t = 0.1$.

In the third scenario, a drop of phase 1 with $R_1 = 0.1$ is surrounded by a drop of phase 2 with $R_2 = 0.2$, both centered at $(0.5, 0.5)$ in a background of phase 3. With the same surface tension coefficients as before, Young-Laplace law gives $P_2 = \sigma_{32}\kappa_{32} = \sigma_{32}/R_2 = 1.5$ and $P_1 = P_2 + \sigma_{12}\kappa_{12} = P_2 + \sigma_{12}/R_1 = 2.5$. This is in agreement with our numerical results at $t = 0.1$, shown in Panels (e) and (f) of Fig. 8. To demonstrate the convergence of the surface tension force calculation, we examine the error in the maximum pressure for this case. In Fig. 9, $E_P = (P_{max} - 2.5)/2.5$ is plotted as a function of mesh resolution, while $\epsilon/\Delta x = 1$ and $\gamma/|\bar{u}|_{max} = 1$ are fixed. It is clear that the surface tension force converges with mesh refinement, for the most part, with a rate between first and second order accuracy. Based on the observations from the convergence rate of the LCSF model in two-phase flows [54], we expect deterioration of the convergence rate at high resolutions when $\epsilon/\Delta x$ is fixed. Indeed, despite being more accurate than the traditional CSF model, similar to CSF, to achieve a first-order or higher convergence rate in two-phase flows, the mesh size must shrink at a higher rate than the interface thickness, ϵ . Another potential reason for this lower convergence rate at the highest resolutions in Fig. 9 is the definition of the error, E_P , which we have used here. This is an l^∞ type norm for the error, which can also bring down the convergence rate.

5.3. Three-phase tessellation

This problem is designed to assess the ability of the coupled N -phase solver in predicting the correct equilibrium configuration at triple junction zones. The initial condition with $\vec{u} = 0$, shown with a plot of $\phi_1 - \phi_2$ in Fig. 10, is designed such that periodic boundary conditions can be used. This allows us to isolate and study triple junctions without having to enforce contact angle boundary conditions at the walls. We test three different combinations for the surface tension coefficients. The domain size is 1×1 , the mesh is 200×200 , all density values are $\rho_1 = \rho_2 = \rho_3 = 1$ and all viscosities are $\mu_1 = \mu_2 = \mu_3 = 10^{-5}$. We fix $\gamma / |\vec{u}|_{max} = 1$ for these simulations. The blue, red, and magenta lines in Figs. 10 and 11 represent contour lines of $\phi_1 = 0.5$, $\phi_2 = 0.5$, and $\phi_3 = 0.5$, respectively.

For the first set of simulations, in accordance with Eq. (24), we use $\epsilon_{pq}\sigma_{pq} = \Delta x$. In the first case, equal surface tension coefficients, $\sigma_{12} = \sigma_{23} = \sigma_{31} = 1$, and thus, equal interfacial thicknesses, $\epsilon_{12} = \epsilon_{23} = \epsilon_{31} = \Delta x$, are used for all pairs of phases. The system quickly

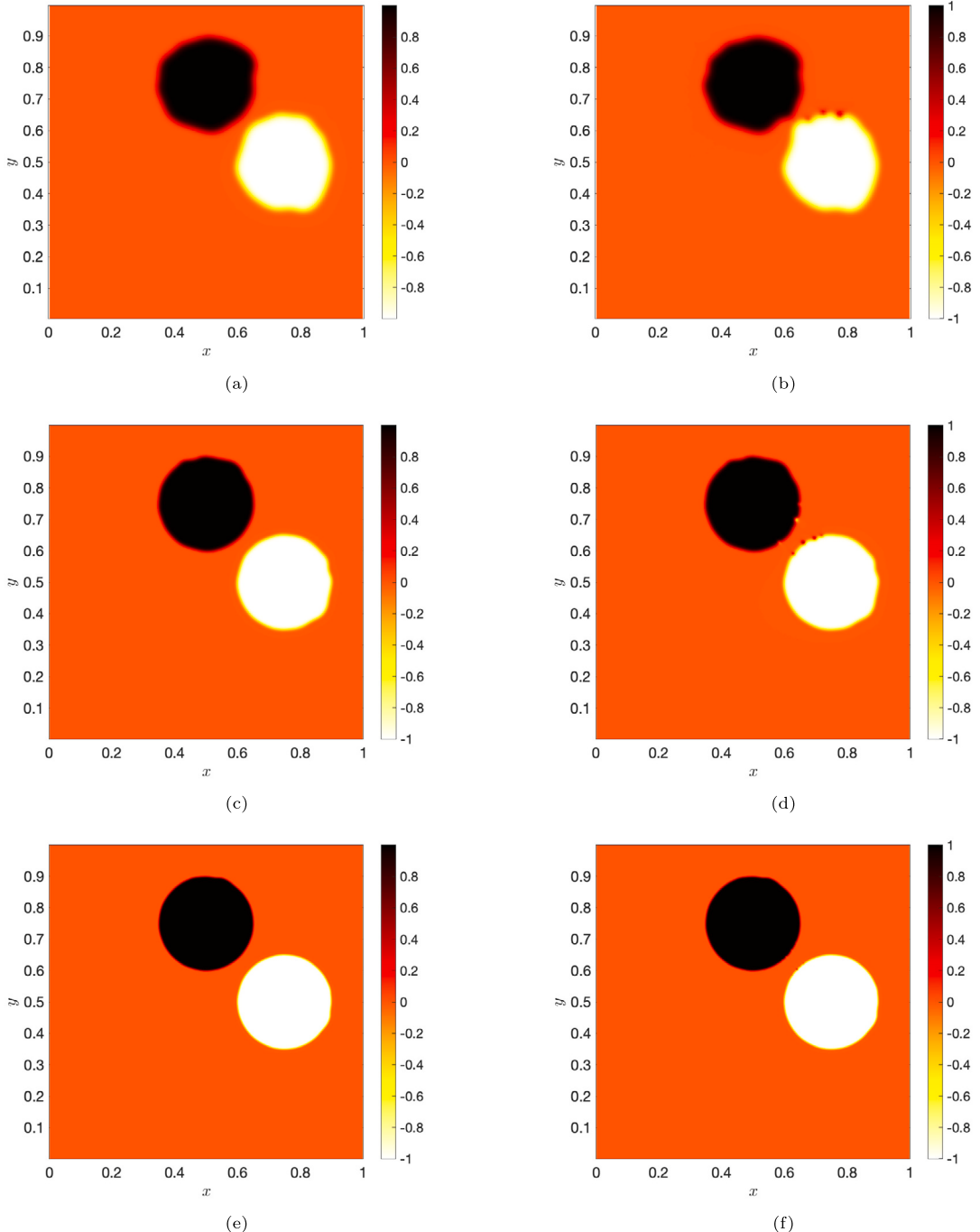


Fig. 6. Plots of $\phi_2 - \phi_1$ at $t = T$ for 2D drops in shear flow simulations using (a) present model on a 128×128 grid, (b) Abadi et al. [33] model on a 128×128 grid, (c) present model on a 256×256 grid, (d) Abadi et al. [33] model on a 256×256 grid, (e) present model on a 512×512 grid, (f) Abadi et al. [33] model on a 512×512 grid.

equilibrates to a state where all of the triple junction points have three 120° angles, and all interfaces are straight lines. This is illustrated in Fig. 11a, where $\phi_1 - \phi_2$ is plotted at $t = 0.2$. In the second case, the surface tension coefficients are given by $\sigma_{12} = 1.0$, $\sigma_{23} = 0.6$, and $\sigma_{31} = 0.8$, and the interfacial parameters are thus $\epsilon_{12} = \Delta x$, $\epsilon_{23} = \Delta x/0.6$, and $\epsilon_{31} = \Delta x/0.8$. In Fig. 11b, the results of the simulations at $t = 0.2$ are shown, wherein 90° equilibrium angles can be seen in phase 3, in agreement with Neumann's law [60]. For the third case, we test $\sigma_{12} = 1.0$, $\sigma_{23} = 0.45$, $\sigma_{31} = 0.45$, and in agreement with Eq. (24), $\epsilon_{12} = \Delta x$, $\epsilon_{23} = \Delta x/0.45$, and $\epsilon_{31} = \Delta x/0.45$. Since $\sigma_{12} > \sigma_{23} + \sigma_{31}$, Eq. (22) cannot be satisfied. Hence, as opposed to the previous two cases, we expect triple junction zones with solutions given by Eq. (12) to not be possible. In the physical limit of sharp interfaces, due to the impossibility of

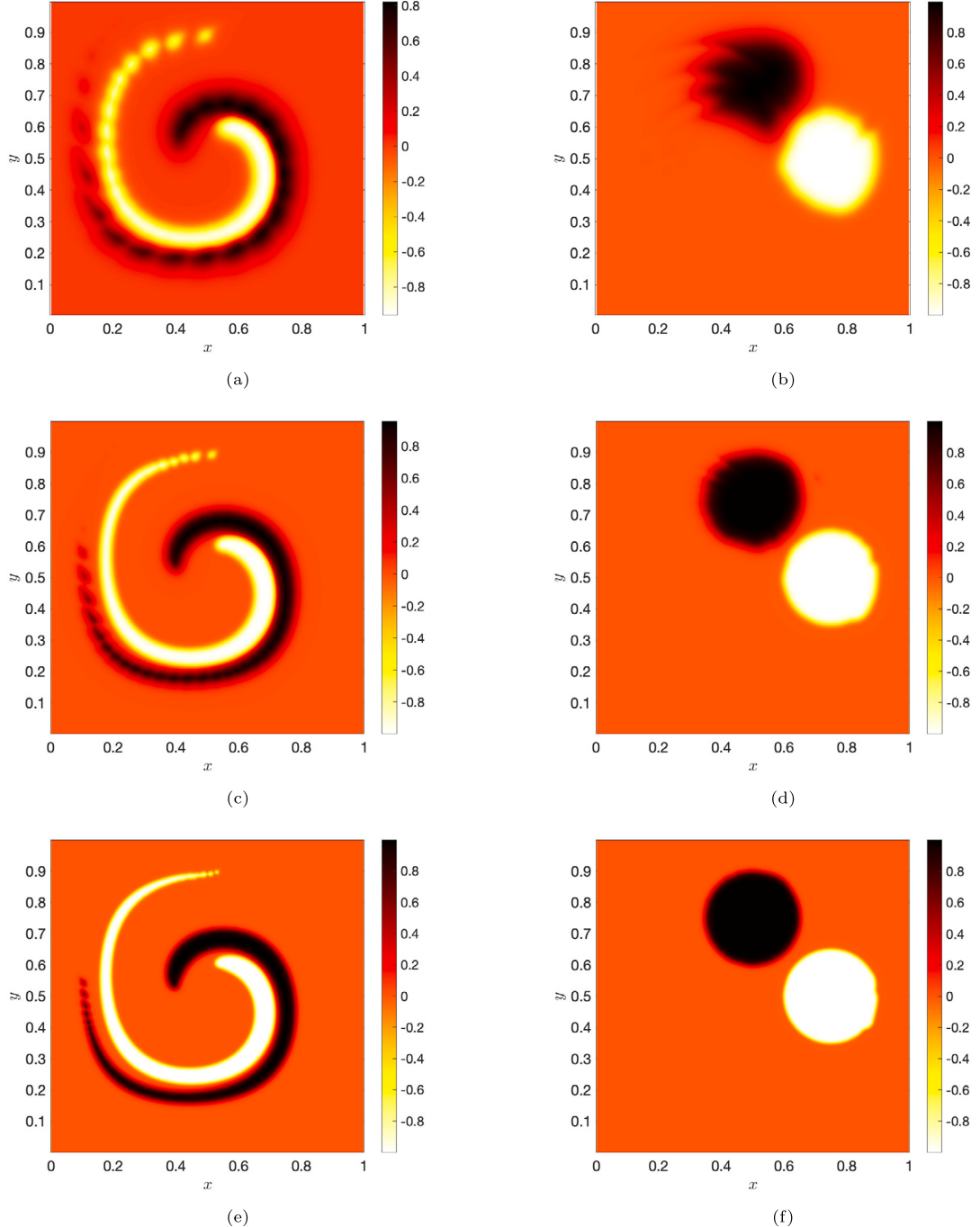


Fig. 7. Plots of $\phi_2 - \phi_1$ for 2D drops in shear flow simulations using present model with unequal interfacial thicknesses of $\epsilon_{12} = \epsilon_{23}/4 = \epsilon_{31}/2 = \epsilon$ on a 128×128 grid at (a) $t = T/2$ and (b) $t = T$, 256×256 grid at (c) $t = T/2$ and (d) $t = T$, and 512×512 grid at (e) $t = T/2$ and (f) $t = T$.

attaining force balance it is impossible for the system to attain a static triple junction zone. Energetically, the system should evolve in a manner to minimize free surface energies. As a result, we expect interfaces between phase 1 and 2 to gradually be replaced by interfaces between either of these phases and phase 3. Indeed, the numerical solution at $t = 3.71$ in Fig. 11c clearly shows how the initially horizontal interfaces between phase 1 and 2 have been replaced by a thick film of phase 3. Moreover, the initially vertical interface between phase 1 and 2 is replaced by a thin film of phase 3, as is evident from Fig. 11d where we have zoomed in onto the center of Fig. 11c. These numerical results thus qualitatively confirm the analytical property of the PDEs explained in Section 2.1, whereby choosing $\epsilon_{pq} \propto 1/\sigma_{pq}$ results in the phase field and momentum transport equations equilibrating to the correct solutions at triple junctions.

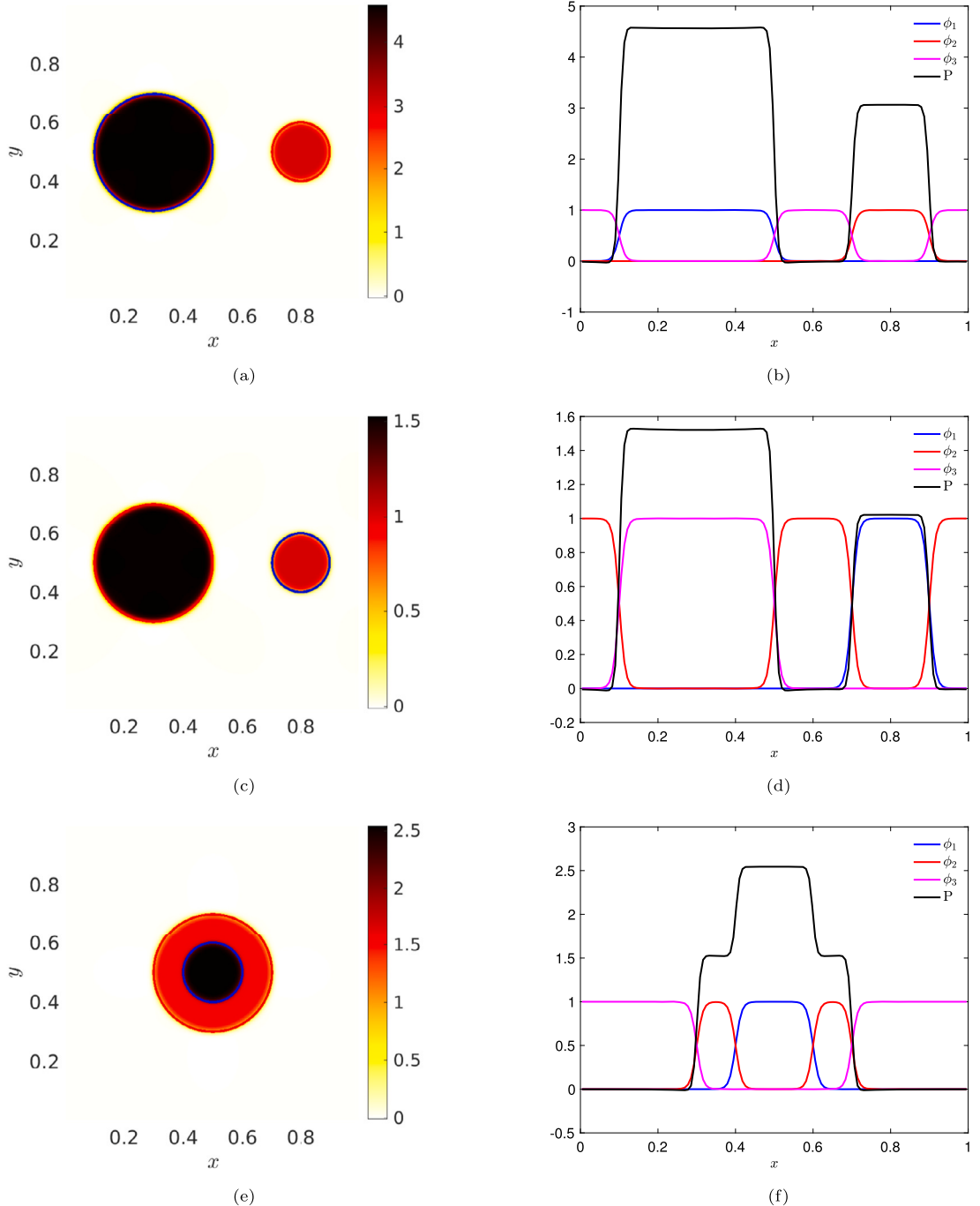


Fig. 8. Results for the surface tension accuracy test, showing the (a) pressure field and (b) phase field variables and pressure at $y = 0.5$, for the first scenario, (c) pressure field and (d) phase field variables and pressure at $y = 0.5$, for the second scenario, and (e) pressure field and (f) phase field variables and pressure at $y = 0.5$, for the third scenario.

To demonstrate the advantage of using $\epsilon \propto 1/\sigma_{pq}$ compared to constant interface thicknesses in attaining the correct equilibrium configuration at triple junctions, we now present the results of simulations of the last two tests with $\epsilon_{pq} = \Delta x$. Fig. 12a shows the solution field at $t = 0.2$ from the simulation with $\sigma_{12} = 1.0$, $\sigma_{23} = 0.6$, and $\sigma_{31} = 0.8$. The predicted equilibrium configuration has approximately three 120° angles at the junction zones, as opposed to the result using $\epsilon \propto 1/\sigma_{pq}$, shown in Fig. 11b, where in agreement with Neumann's law, 90° angles are predicted in phase 3. Similarly, Fig. 12b shows the result of a simulation with $\epsilon_{pq} = \Delta x$ at $t = 3.71$ for $\sigma_{12} = 1.0$, $\sigma_{23} = 0.45$, $\sigma_{31} = 0.45$. Again, 120° angles are predicted, as opposed to the correct separation behavior predicted in the simulation results shown in Figs. 11c and 11d. To explain, according to Section 2.1, Eq. (14) will be an

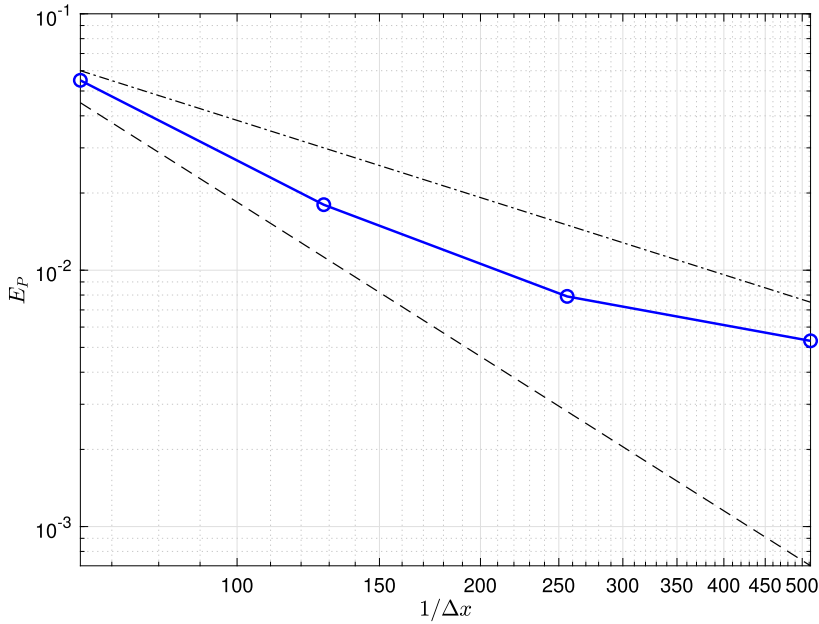


Fig. 9. Error in calculation of the pressure jump for the third scenario of the surface tension accuracy tests plotted as a function of resolution. Dash-dotted and dashed lines represent first and second order convergence rates, respectively.

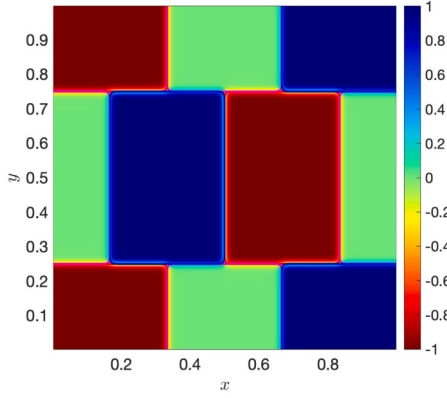


Fig. 10. Initial condition for the three-phase tessellation problem demonstrated via a plot of the $\phi_1 - \phi_2$ field.

equilibrium solution to the phase field equation when the relation between the interfacial thickness parameters and triple point angles given by Eq. (18) is satisfied. As such, as explained in Section 2.2, for this problem where we are concerned with correct predictions of the triple junction angles, it is required to trade off accuracy in two-phase regions (thicker interfaces) to gain accuracy at the triple junctions by using $\epsilon \propto 1/\sigma_{pq}$ instead of constant ϵ_{pq} .

5.4. Floating liquid lens

This is a standard test to study the model's capability in predicting the equilibrium configuration of a three-phase system consisting of an oil drop sandwiched between air and water layers [62,60,27,32]. The oil drop is initially circular with a radius $R_o = 0.008$ m, and is placed at the center of the $0.08 \text{ m} \times 0.032$ domain. The bottom half of the domain is otherwise filled with water and the top half with air. We follow [27] in specifying the initial conditions for the phase field variables. The initial condition is shown in Fig. 13a, where $\phi_w - \phi_o$ is shown and the red, blue, and magenta lines represent contour lines of $\phi_w = 0.5$, $\phi_o = 0.5$, and $\phi_a = 0.5$, respectively. Periodic boundary conditions are employed in the x direction, while no-slip boundary condition is enforced for the top and bottom walls. A 200×80 mesh is used to explore the equilibrium configurations predicted by the simulations for different values of gravity and surface tension coefficients. We use uniform interfacial thicknesses of $\epsilon = \Delta x$ for all phase pairs, and fix $\gamma/|\vec{u}|_{max} = 1$ for the simulations in this section.

Let us first examine results from simulations with $\bar{g} = 0$. In the absence of gravity, there are analytical relations that hold for the equilibrium configuration [33,38]. Fig. 13b schematically shows the geometrical features that we measure and compare against

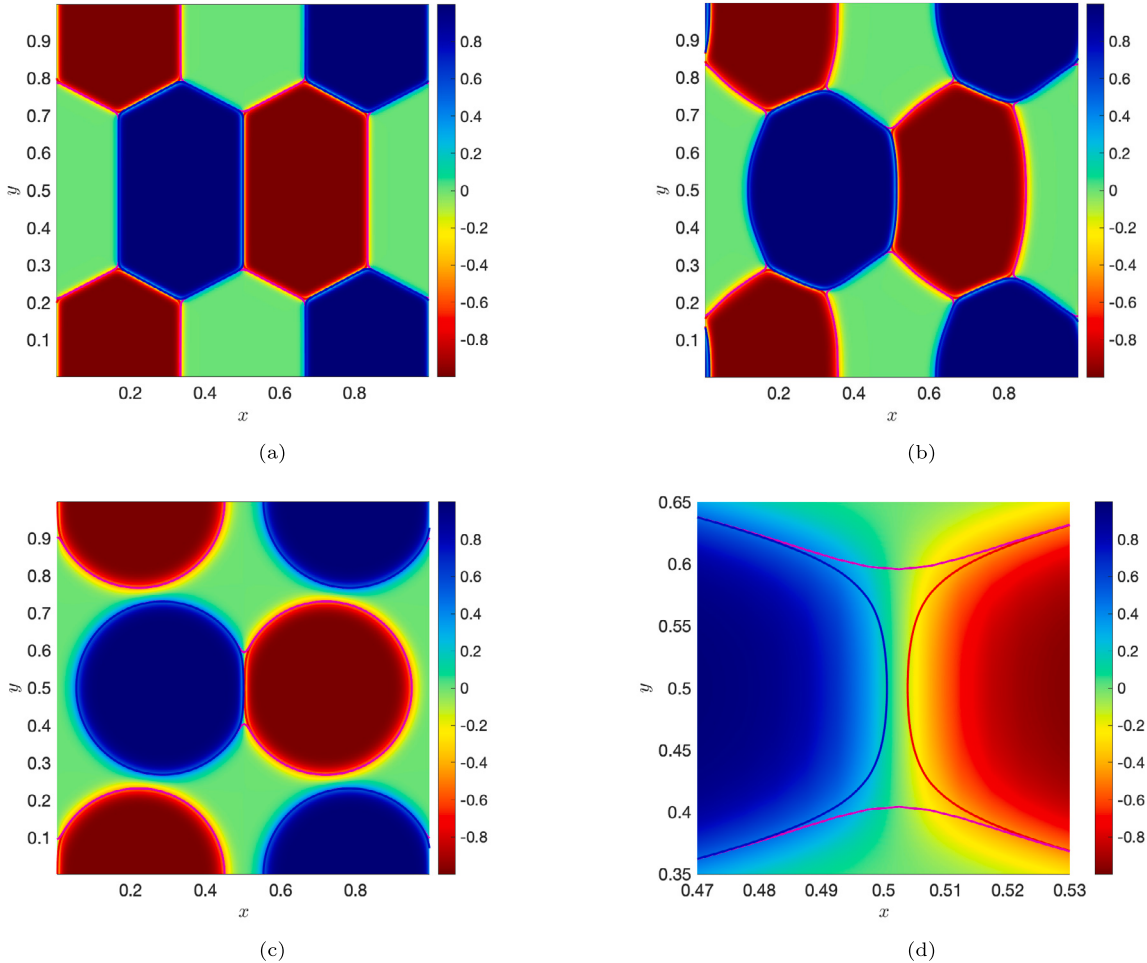


Fig. 11. Plots of $\phi_1 - \phi_2$ for the three-phase tessellation case at long times when the triple junctions have attained their equilibrium configuration for (a) $\sigma_{12} = \sigma_{23} = \sigma_{31} = 1$, and $\epsilon_{12} = \epsilon_{23} = \epsilon_{31} = \Delta x$, (b) $\sigma_{12} = 1.0$, $\sigma_{23} = 0.6$, and $\sigma_{31} = 0.8$, and $\epsilon_{12} = \Delta x$, $\epsilon_{23} = \Delta x/0.6$, $\epsilon_{31} = \Delta x/0.8$, and (c) $\sigma_{12} = 1.0$, $\sigma_{23} = 0.45$, $\sigma_{31} = 0.45$, and $\epsilon_{12} = \Delta x$, $\epsilon_{23} = \Delta x/0.45$, and $\epsilon_{31} = \Delta x/0.45$. Panel (d) is a close-up view of Panel (c), showing how phase 1 and 2 have separated in the middle of the domain.

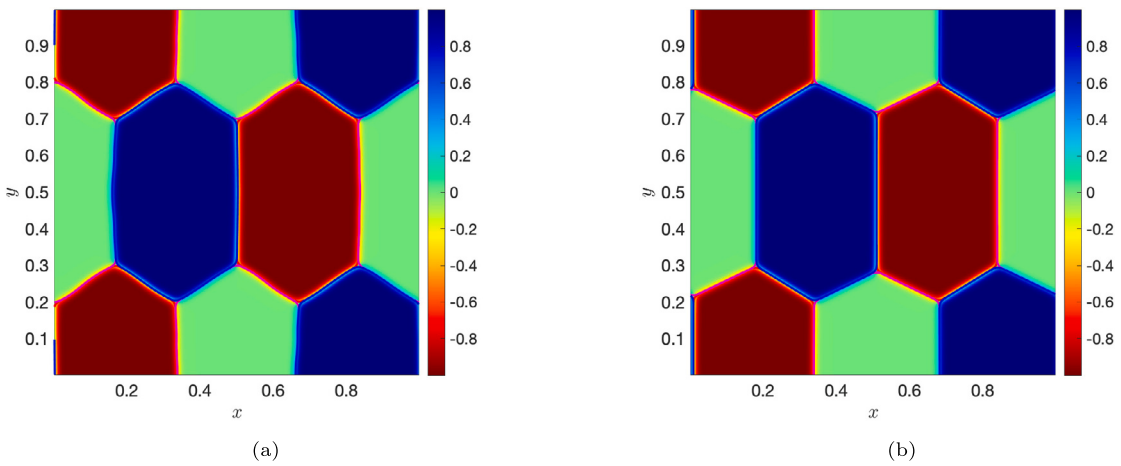


Fig. 12. Plots of $\phi_1 - \phi_2$ for the three-phase tessellation case at long times when the triple junctions have attained their equilibrium configuration for (a) $\sigma_{12} = 1.0$, $\sigma_{23} = 0.6$, and $\sigma_{31} = 0.8$, and $\epsilon_{12} = \epsilon_{23} = \epsilon_{31} = \Delta x$, and (b) $\sigma_{12} = 1.0$, $\sigma_{23} = 0.45$, $\sigma_{31} = 0.45$, and $\epsilon_{12} = \epsilon_{23} = \epsilon_{31} = \Delta x$.

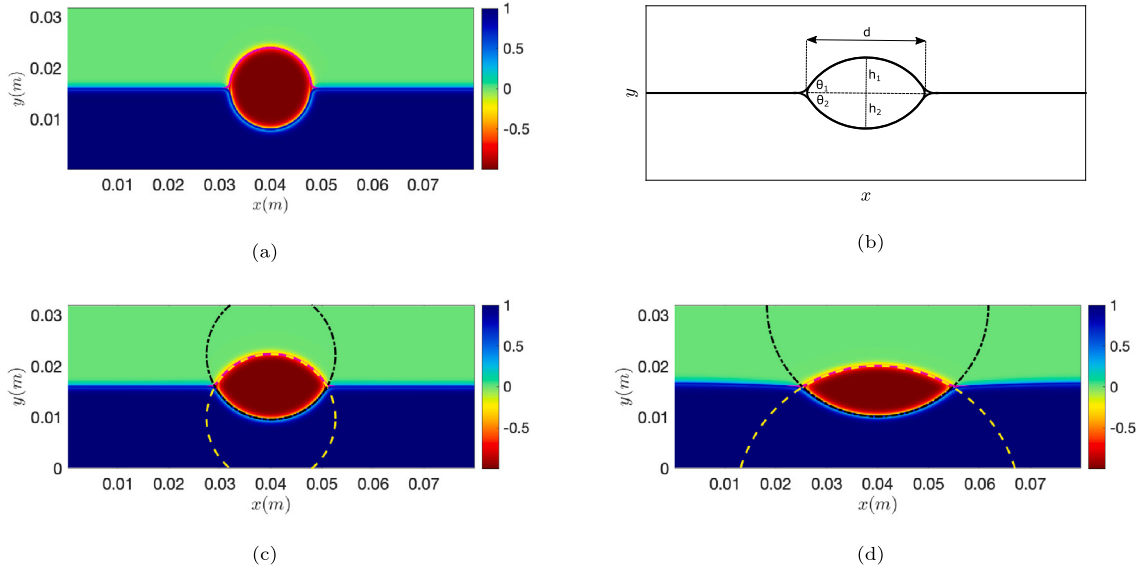


Fig. 13. (a) The initial condition and domain for the floating lens simulations (b) schematic of the measured geometric quantities (c) $\phi_w - \phi_o$ for the gravity-free floating lens simulations at equilibrium for equal surface tension coefficients of $\sigma_{wa} = \sigma_{ao} = \sigma_{ow} = 0.055 \text{ kg/s}^2$ and (d) realistic surface tension values of $\sigma_{wa} = 0.0728 \text{ kg/s}^2$, $\sigma_{ao} = 0.055 \text{ kg/s}^2$, and $\sigma_{ow} = 0.04 \text{ kg/s}^2$. Two circular arcs in Panels (c) and (d) demonstrate the constant curvature interfaces that are predicted in the absence of gravity.

Table 2

Relative errors in the prediction of the equilibrium geometrical features shown schematically in Fig. 13b for the gravity-free simulations (shown in Figs. 13c and 13d).

surface tension coefficients	$E(\theta_1)$	$E(\theta_2)$	$E(d)$	$E(h_1)$	$E(h_2)$
$\sigma_{wa} = \sigma_{ao} = \sigma_{ow} = 0.055 \text{ kg/s}^2$	0.8%	0.8%	0.9%	0.05%	0.05%
$\sigma_{wa} = 0.0728 \text{ kg/s}^2$, $\sigma_{ao} = 0.055 \text{ kg/s}^2$, $\sigma_{ow} = 0.04 \text{ kg/s}^2$	3%	10.75%	5.75%	2.39%	6.83%

the theory to assess the accuracy of our model. The material properties are $\rho_o = 577 \text{ kg/m}^3$ and $\mu_o = 9.15 \times 10^{-2} \text{ kg/ms}$ for oil, $\rho_w = 998.2 \text{ kg/m}^3$ and $\mu_w = 10^{-3} \text{ kg/ms}$ for water, and $\rho_a = 1.204 \text{ kg/m}^3$ and $\mu_a = 1.78 \times 10^{-5} \text{ kg/ms}$ for air. For our first test, we use equal surface tension values of $\sigma_{wa} = \sigma_{ao} = \sigma_{ow} = 0.055 \text{ kg/s}^2$. The equilibrium configuration from this simulation is shown in Fig. 13c. Two overlaying circles with equal radii are also drawn to show that in the absence of gravity, the surfaces assume uniform curvature profiles, in accordance with the theory [60]. In the next test, and for the remainder of numerical simulations in this section, we use pairwise surface tension coefficients of $\sigma_{wa} = 0.0728 \text{ kg/s}^2$, $\sigma_{ao} = 0.055 \text{ kg/s}^2$, and $\sigma_{ow} = 0.04 \text{ kg/s}^2$. The gravity-free equilibrium configuration for these surface tension values is shown in Fig. 13d, accompanied by the two overlaying circles which in line with the theory of [60], indicate constant curvature profiles. More quantitatively, we can examine values for the geometric quantities θ_1 , θ_2 , d , h_1 , and h_2 , shown schematically in Fig. 13b, and compute their error with respect to the theory. According to Neumann's law, the contact angles θ_1 and θ_2 are related to surface tension values via

$$\cos(\theta_1) = \frac{\sigma_{ao}^2 + \sigma_{wa}^2 - \sigma_{ow}^2}{2\sigma_{ao}\sigma_{wa}}, \quad \cos(\theta_2) = \frac{\sigma_{ow}^2 + \sigma_{wa}^2 - \sigma_{ao}^2}{2\sigma_{ow}\sigma_{wa}}, \quad (30)$$

from which the lens length is

$$d = 2 \sqrt{\frac{A}{\sum_{i=1}^2 \frac{1}{\sin(\theta_i)} \left(\frac{1}{\sin \theta_i} - \cos \theta_i \right)}}, \quad (31)$$

where A is the lens area [38]. The lens heights are then given by

$$h_i = \left(\frac{d}{2} \right) \frac{1 - \cos \theta_i}{\sin \theta_i}, \quad i = 1, 2. \quad (32)$$

Table 2 presents the relative errors in the predictions from the gravity-free simulations shown in Figs. 13c and 13d against the theory (Eqs. (30)-(32)). Despite the modest resolution of the simulations and the errors involved in computing the geometric quantities, the predictions boast high levels of accuracy.

We now turn our focus to simulations with gravity. As gravity is increased to $|\vec{g}| = 2 \text{ m/s}^2$, 5 m/s^2 , 7.5 m/s^2 , and 9.8 m/s^2 , Fig. 14 shows the equilibrium profiles of the oil drops after they have spread out. During this process, the interfaces flatten and the drops transform into puddles. In the asymptotic limit of large $|\vec{g}|$, where gravity dominates capillarity, the Langmuir-de Gennes theory

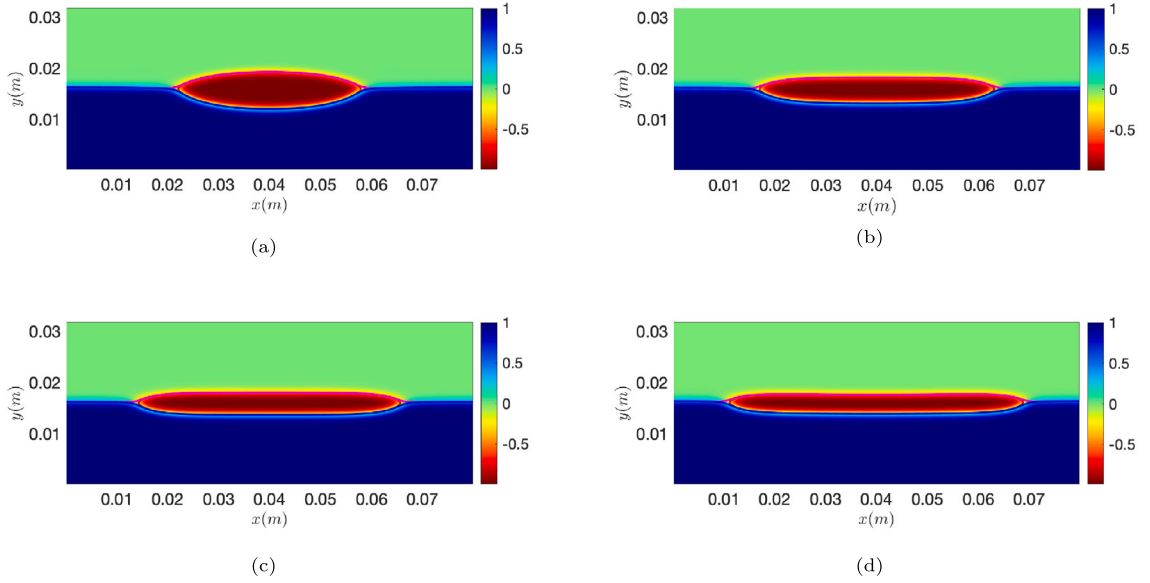


Fig. 14. Plots of $\phi_w - \phi_o$ at long times for the floating lens case when the system has attained an equilibrium state for (a) $|\vec{g}| = 2 \text{ m/s}^2$, (b) $|\vec{g}| = 5 \text{ m/s}^2$, (c) $|\vec{g}| = 7.5 \text{ m/s}^2$, and (d) $|\vec{g}| = 9.8 \text{ m/s}^2$.

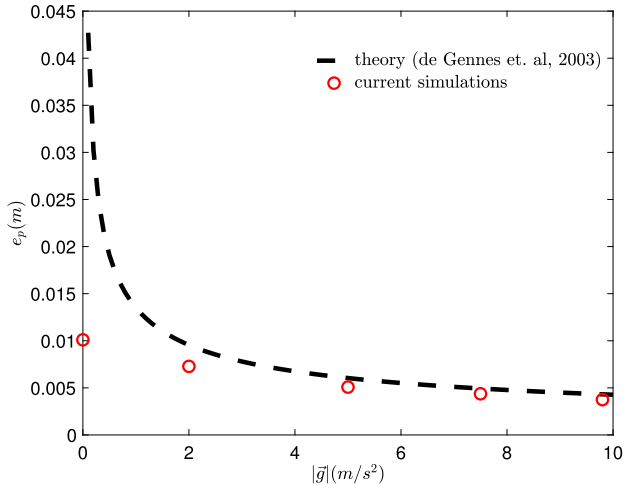


Fig. 15. Thickness of the floating lens puddle at equilibrium predicted by our simulations compared against theory [60] for various values of gravitational acceleration.

[62,60] provides the thickness of the puddle, e_p , as a function of the material properties and gravitational acceleration,

$$e_p = \sqrt{\frac{2(\sigma_{ao} + \sigma_{ow} - \sigma_{wa})\rho_w}{\rho_o(\rho_w - \rho_o)|\vec{g}|}}. \quad (33)$$

In Fig. 15, we compare the puddle thickness from our simulations, measured at the center of the puddle ($x = 0.04 \text{ m}$), against the Langmuir-de Gennes theory. As explained by [24,27], the asymptotic theory holds for $|\vec{g}| > 5 \text{ m/s}^2$. Indeed, we observe that our numerical predictions match the theory quite well in this limit.

5.5. A dynamic buoyancy-driven 2D problem

We now move on to a two-dimensional dynamic problem inspired by a case used in [27]. In contrast to the 4-phase test used in [27] though, we study a three-phase system where two circular oil drops of the same phase are initiated in a water pool and in the air resting above the pool. Fig. 16 shows the initial condition of the system, where $\phi_w - \phi_o$ is plotted. The system is initially stationary. The domain is $0.008 \text{ m} \times 0.008 \text{ m}$, with slip boundary conditions used everywhere for velocity and Neumann boundary conditions employed for phase field variables. The $R_o = 0.001 \text{ m}$ oil drops are placed at $(0.0035 \text{ m}, 0.0065 \text{ m})$ and $(0.0045 \text{ m}, 0.0015 \text{ m})$ at $t = 0$.

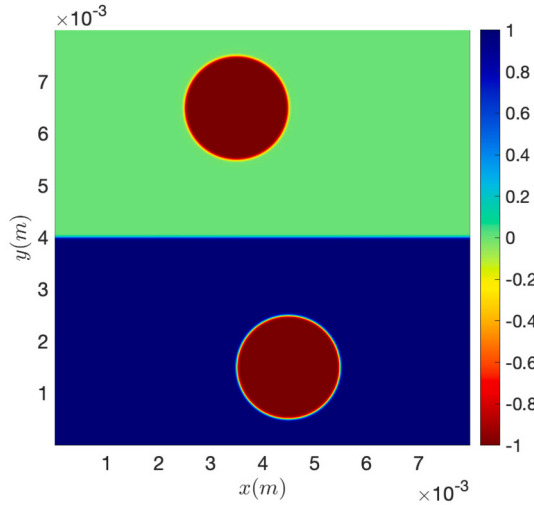


Fig. 16. Plot of $\phi_w - \phi_o$ at $t = 0$ s, showing the initial condition for the dynamic buoyancy-driven problem.

All material properties match those of the floating lens tests (Section 5.4, with non-equal surface tension coefficients), and gravity is $|\vec{g}| = 9.8 \text{ m/s}^2$.

Let us first examine the results of simulations with various levels of resolution using $\epsilon_{pq} = \Delta x$ for all phase pairs and $\gamma/|\vec{u}|_{max} = 1$. Fig. 17 depicts the evolution of the system in time for simulations on 128×128 (left panels) and 256×256 (right panels) grids. Due to buoyancy effects, the oil drop in air falls while the oil drop in water rises. We observe that at these two low resolutions, the falling drop impacts the pool first and then coalesces with the rising drop. We observe entrapment of air bubbles and water drops inside the large oil that is formed after coalescence. This is because similar to the simulations performed by [27], the thin air film under the falling drop and the thin water film above the rising drop are not fully squeezed out, the mass of which are converted to air bubbles and water drops. As a result, at later times, as shown in Panels (g) and (h), the system consists of a floating oil drop resting on top of the water pool, with entrapped air bubbles and water drops that are slowly rising and falling in response to buoyancy. As we will show below via higher resolution simulation, many of the features observed in these coarse simulations are artificial.

Fig. 18 shows results from high-resolution simulations on 512×512 (left panels) and 768×768 (right panels) grids. While the top oil drop falls in air and the bottom oil drop rises in water, there is a striking difference between the high resolution results in Fig. 18 and the low resolution results in Fig. 17. Namely, the falling oil drop bounces off the water pool in both simulations. Computing the velocity of the drop upon impact using $h \approx 0.0015 \text{ m}$, the falling height of the drop, we obtain $U \approx \sqrt{2|\vec{g}|h} = 0.17 \text{ m/s}$. Indeed, based on studies of drop-pool impact events [63–65], bouncing off the pool is expected for such a low Weber number impact ($We = \rho_o U^2 R_o / \sigma_{ao} \approx 0.3$). It is a testament to the accuracy of our N -phase flow model that we converge to the correct physical behavior at the two higher resolutions. By comparing the left and right panels in Fig. 18, it is clear that the results are mesh converged up until $t = 0.0419 \text{ s}$ (panels c and d). After this time, as shown in panels (e) and (g), the 512×512 simulation suffers from a minor artificial effect. Specifically, small water drops that are remnants of the draining water film persist on the initially-rising oil drop after it has risen to the pool surface. Clearly, panels (f) and (h) show that these artificial effects disappear with mesh refinement. These results confirm that our coupled N -phase model converges to the correct physical behavior and is robust and accurate in the face of complex dynamic problems involving large density ratios.

Finally, to demonstrate the tradeoff in using constant interface thickness, $\epsilon_{pq} = \Delta x$, versus $\epsilon_{pq} \propto 1/\sigma_{pq}$ (Section 2.2), we now present the results from a 512×512 simulation with $\epsilon_{pq} \propto 1/\sigma_{pq}$. Specifically, while keeping everything the same, we use $\epsilon_{wa} = \Delta x$, $\epsilon_{ao} = (0.0728/0.055)\Delta x = 1.32\Delta x$, and $\epsilon_{ow} = (0.0728/0.04)\Delta x = 1.82\Delta x$ in Eq. (2). The simulation results are shown in Fig. 19, where in contrast to the constant $\epsilon_{pq} = \Delta x$ simulation results at this resolution (left panels of Fig. 18), the top oil drop does not bounce off of the pool and instead coalesces with the bottom oil drop. There are also many artificial drops and bubbles present in the large oil drop after coalescence. As such, as explained in Section 2.2, for such dynamic problems where the prediction at the triple junction zones is not as critical, it is advantageous to minimize the interfacial thicknesses and use constant ϵ_{pq} values, enforced by the mesh size.

5.6. Bubble rise in stratified layers

This three-dimensional test is adopted from [22]. We study the rise of a gas bubble in a stratified system consisting of two immiscible liquid layers. The bubble is released in the heavier bottom liquid layer and rises upwards due to buoyancy. Depending on the size of the bubble, it either becomes entrapped at the liquid-liquid interface or penetrates into the lighter top liquid layer. Because of their small volume, small bubbles do not experience sufficient buoyancy forces to overcome the surface tension forces at the interface between the two liquids. On the other hand, for sufficiently large bubbles, the buoyancy force can overcome the surface tension between the bubble and the heavy liquid, allowing for the bubble to penetrate into the lighter liquid medium.

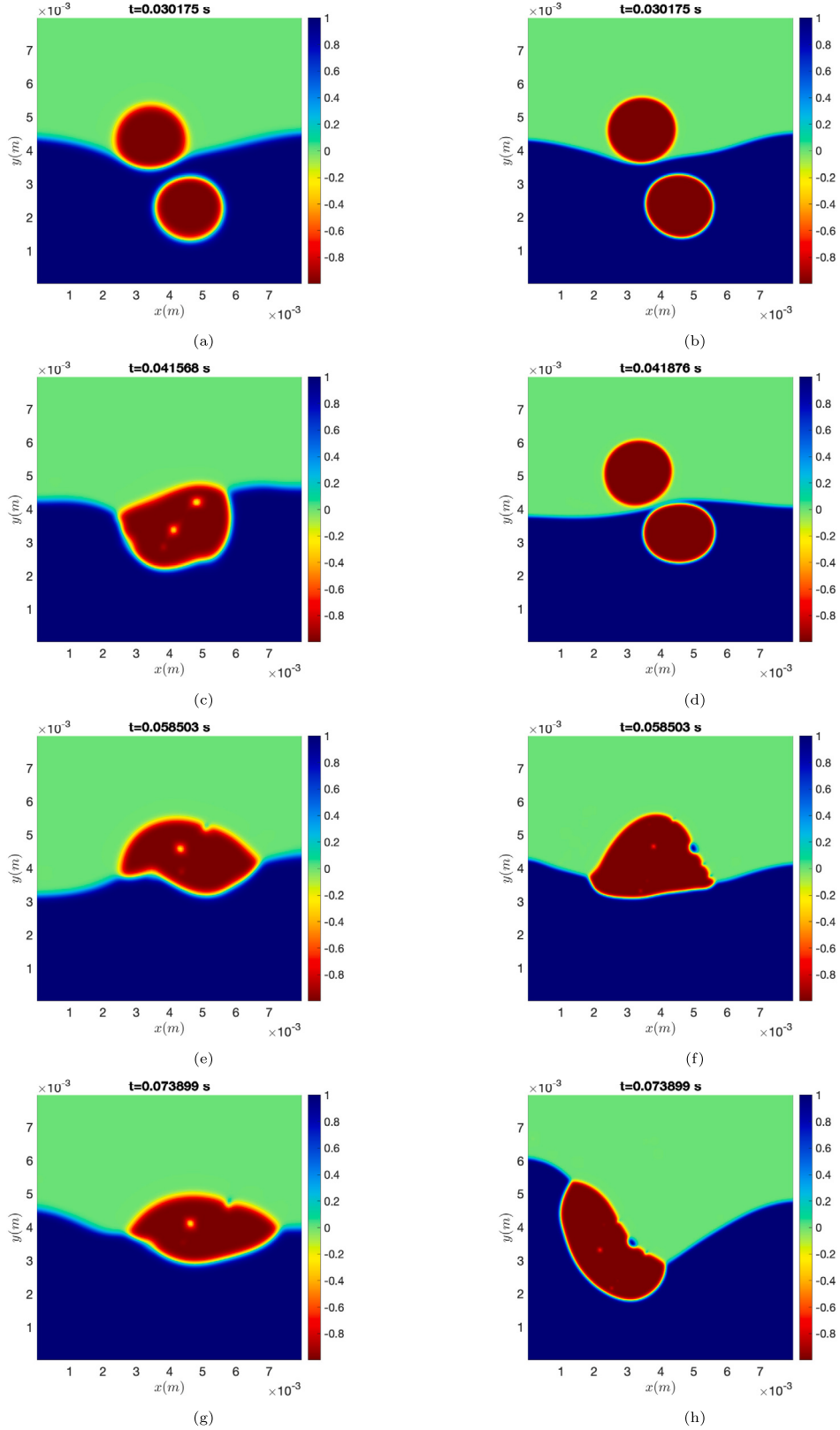


Fig. 17. Plots of $\phi_{\text{w}} - \phi_o$ at different times for simulations with $\epsilon_{\text{ao}} = \epsilon_{\text{ow}} = \epsilon_{\text{wo}} = \Delta x$ of the dynamic problem of two oil drops interacting with a water pool. Left panels (a, c, e, and f) depict results from the 128×128 simulation, while right panels (b, d, f, and h) depict results from the 256×256 simulation.

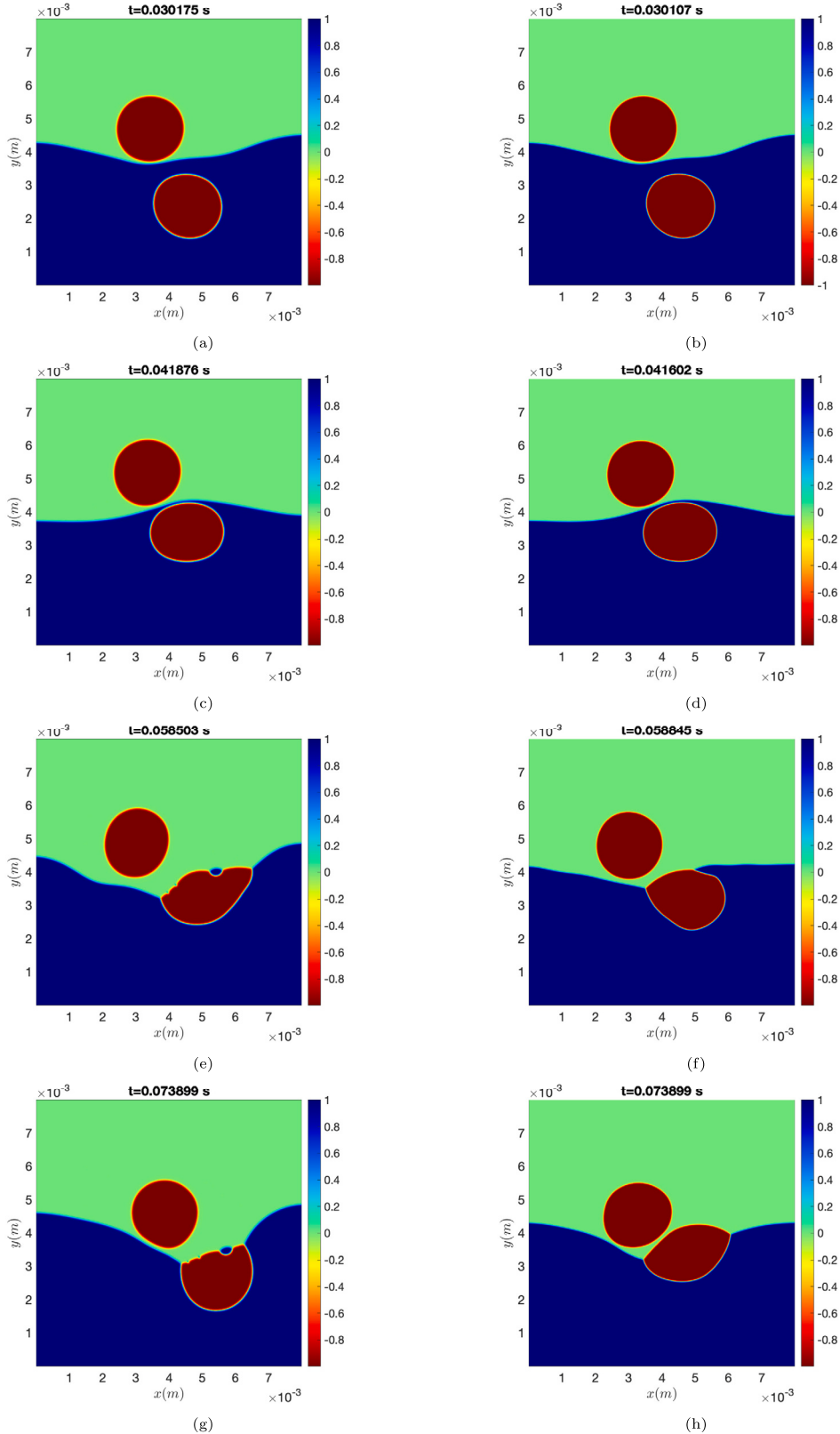


Fig. 18. Plots of $\phi_w - \phi_o$ at different times for simulations with $\epsilon_{wo} = \epsilon_{ow} = \epsilon_{wo} = \Delta x$ of the dynamic problem of two oil drops interacting with a water pool. Left panels (a, c, e, and f) depict results from the 512×512 simulation, while right panels (b, d, f, and h) depict results from the 768×768 simulation.

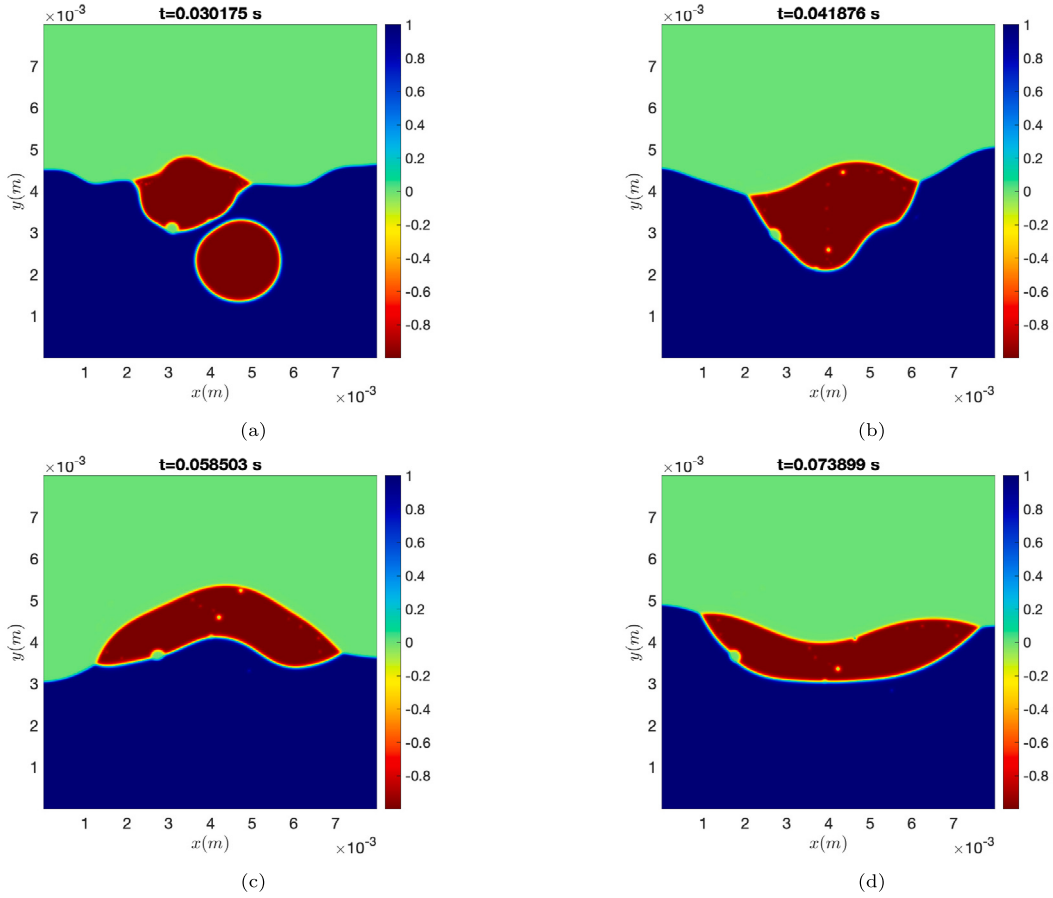


Fig. 19. Plots of $\phi_w - \phi_o$ at different times for 512×512 simulations with $\epsilon_{wa} = \Delta x$, $\epsilon_{ao} = 1.32\Delta x$, and $\epsilon_{ow} = 1.82\Delta x$ of the dynamic problem of two oil drops interacting with a water pool.

We examine two cases involving a small bubble and a large bubble. The system is initially stationary in both cases. Slip boundary conditions are used everywhere for velocity and Neumann boundary conditions are employed for phase field variables. The material properties are $\rho_1 = 1000 \text{ kg/m}^3$ and $\mu_1 = 0.1 \text{ kg/ms}$ for the light liquid, $\rho_2 = 1200 \text{ kg/m}^3$ and $\mu_2 = 0.15 \text{ kg/ms}$ for the heavy liquid, and $\rho_3 = 1 \text{ kg/m}^3$ and $\mu_3 = 10^{-4} \text{ kg/ms}$ for the gas inside the bubble. The pairwise surface tension coefficients are $\sigma_{12} = 0.05 \text{ kg/s}^2$, $\sigma_{23} = \sigma_{31} = 0.07 \text{ kg/s}^2$, and gravity is downwards with $|\vec{g}| = 9.8 \text{ m/s}^2$. Based on the theory presented by [60], bubbles larger than the critical radius of

$$R_c \approx \sqrt{\frac{3\sigma_{23}}{2(\rho_1 - \rho_3)g}}, \quad (34)$$

can penetrate through the interface, while bubbles smaller than R_c are entrapped at the liquid-liquid interface. For the material properties chosen here, $R_c \approx 2.8 \times 10^{-3} \text{ m}$. A $64 \times 128 \times 64$ mesh is used and for the phase field parameters, we use $\epsilon_{pq} = \Delta x$ for all phase pairs and $\gamma/|\vec{u}|_{max} = 1$.

For the first case, the domain is $0.008 \text{ m} \times 0.0016 \text{ m} \times 0.008 \text{ m}$, filled with a layer of light liquid of phase 1 on top of a layer of heavy liquid of phase 2. The bottom layer has a height of $h = 0.005 \text{ m}$. A gas bubble of phase 3 with radius $R = 0.001 \text{ m}$ is placed inside the heavy liquid medium at $(0.004 \text{ m}, 0.002 \text{ m}, 0.004 \text{ m})$ at $t = 0$. Fig. 20 depicts the results of the simulation for this case as a function of time, by plotting the $\phi_1 = 0.5$ and $\phi_3 = 0.5$ isosurfaces in green and red, respectively. Since $R < R_c$ for this case, we expect the bubble to be entrapped at the liquid-liquid interface. Indeed, the simulation results shown in Fig. 20 are in agreement with this expectation.

For the second case, the domain is $0.024 \text{ m} \times 0.0048 \text{ m} \times 0.024 \text{ m}$, filled with a layer of light liquid of phase 1 on top of a layer of heavy liquid of phase 2. The bottom layer has a height of $h = 0.015 \text{ m}$. A gas bubble of phase 3 with radius $R = 0.003 \text{ m}$ is placed inside the heavy liquid medium at $(0.012 \text{ m}, 0.006 \text{ m}, 0.012 \text{ m})$ at $t = 0$. Fig. 21 depicts the results of the simulation for this case as a function of time, by plotting the $\phi_2 = 0.5$ and $\phi_3 = 0.5$ isosurfaces in green and red, respectively. Since $R > R_c$ for this case, we expect the bubble to penetrate through the liquid-liquid interface into the lighter top liquid. The simulation results shown in Fig. 21 are in agreement with this expectation.

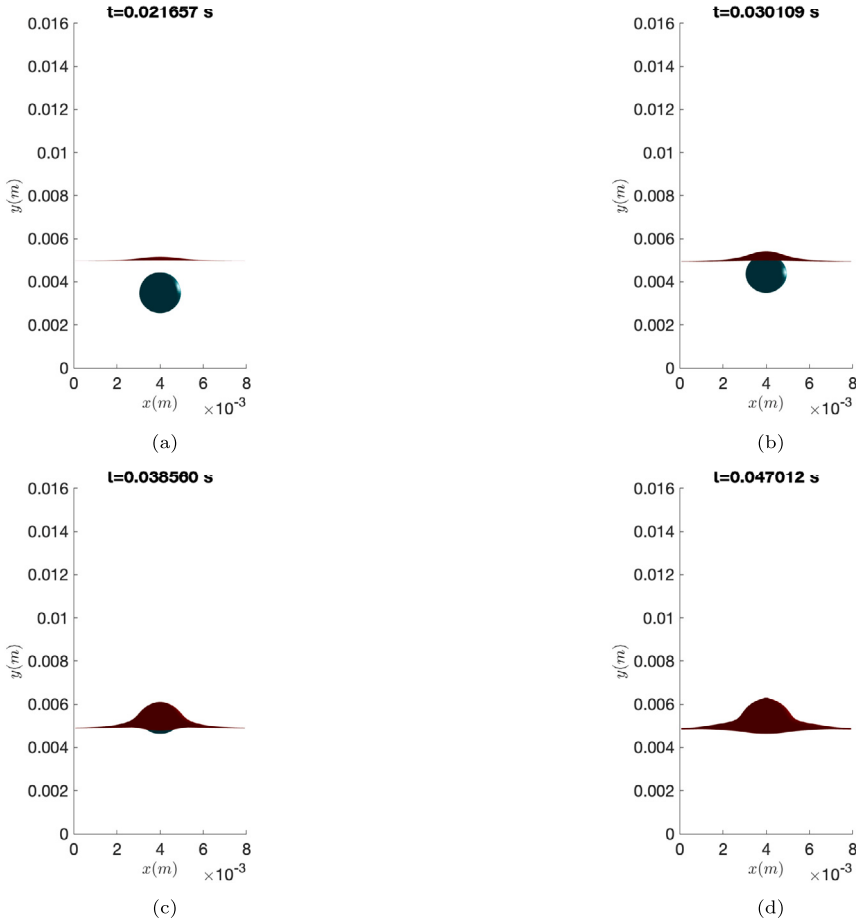


Fig. 20. Evolution of the system for simulations of the first case of bubble rise in stratified layers shown with $\phi_1 = 0.5$ and $\phi_3 = 0.5$ isosurfaces, plotted in green and red, respectively. In accordance with theory, the bubble is trapped at the liquid-liquid interface [60].

6. Summary

This work presented a second-order phase field approach for simulation of N -phase flows. The phase field model consists of N equations governing the N phases, and is (1) in conservative form, (2) reduction consistent, (3) symmetric with respect to the phases, (4) conserves the total volume at all points in space at all times without the need for Lagrange multipliers, and (5) allows for different interfacial thicknesses, given by ϵ_{pq} , between different phases. This is made possible by the novel idea of computing and using pairwise volume fractions and normal vectors. Using second order central differences in space on a Cartesian grid, we demonstrated that the proposed model inherits the boundedness properties of its two-phase predecessor, introduced in [52].

For coupling to momentum transport, the two-phase mass-momentum consistent model introduced in [53] was extended to N -phase flows. The choice of nondissipative central schemes in space allows the N -phase flow solver to also inherit the conservation properties of its two-phase predecessor, rendering it the first N -phase flow solver that conserves mass, momentum and kinetic energy (in the absence of capillary and viscous forces) in the continuous and discrete sense. For calculation of surface tension forces, we took advantage of the pairwise volume fractions and normal vectors to devise a new surface tension model for N -phase flows, extending the localized continuum surface force model (LCSF) introduced in [54] to N -phase flows. With this surface tension model and with the choice of ϵ_{pq} proportional to $1/\sigma_{pq}$, we analytically proved that the fully-coupled N -phase flow model has the theoretical property of achieving the correct equilibrium configuration at the triple junction zones. We explained how this introduces a tradeoff in choosing the values of the interfacial thickness parameters. Specifically, since the magnitude of the interfacial thickness parameters is limited by mesh resolution, one can either sacrifice some accuracy in two-phase regions but gain accuracy in triple junction zones by adopting $\epsilon_{pq} \propto 1/\sigma_{pq}$ or forgo the theoretical property given by the model at triple junction zones to minimize the interfacial thicknesses as much as possible by adopting $\epsilon_{pq} = \text{const} \sim \Delta x$. We demonstrated this tradeoff in practice by performing multiple comparisons in our numerical tests.

We used several numerical tests to assess the phase field model, the surface tension force model, and the fully coupled N -phase flow solver. First, we used an extension of the well-known drop in shear flow case to demonstrate the phase field model's accuracy and convergence rate. Using this test, we compared our model to our implementation of two state-of-the-art second-order conservative

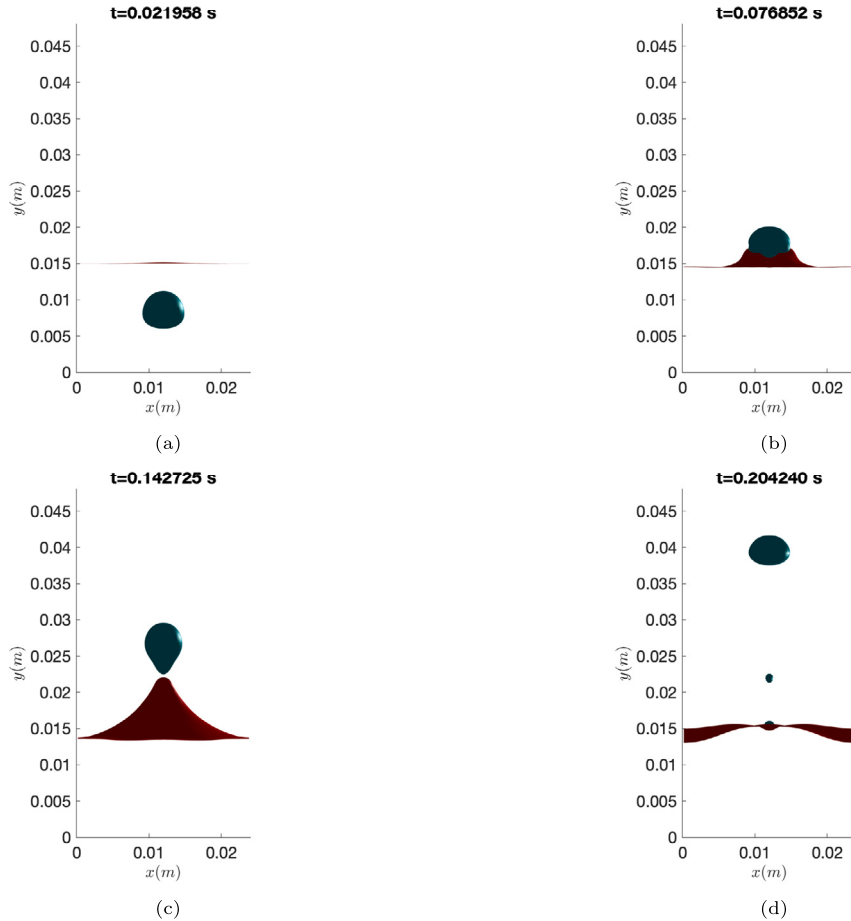


Fig. 21. Evolution of the system for simulations of the second case of bubble rise in stratified layers shown with $\phi_2 = 0.5$ and $\phi_3 = 0.5$ isosurfaces, plotted in green and red, respectively. The bubble is predicted to pass through the liquid-liquid interface, in agreement with the theory [60].

phase field models from the literature [33,35]. We observed that in contrast to their models, our model avoids the issue of artificial creation of three-phase zones, while yielding bounded phase field variables and boasting higher accuracy overall. After assessing the accuracy of our proposed surface tension model, we presented a novel test of three-phase tessellations, which allowed us to study triple junction zones in 2D periodic domains. We observed that by using interfacial thickness parameters inversely proportional to the surface tension coefficients, the fully coupled N -phase solver correctly predicts the triple junction zones' equilibrium configurations, even for scenarios involving total wetting. Finally, by using multiple practical tests in 2D and 3D, such as problems involving floating lenses, and two dynamic problems with drop-pool interactions and bubbles rising in stratified layers, we demonstrated that the fully coupled N -phase solver is robust, convergent, and predicts physically accurate results for both steady and dynamic problems.

CRediT authorship contribution statement

Shahab Mirjalili: Methodology, Analysis, Derivation, Software, Visualization, Investigation, Data curation, Writing-Original draft preparation, Validation. **Ali Mani:** Conceptualization, Derivation, Supervision, Reviewing, and Editing.

Declaration of competing interest

The authors declare the following financial interests/personal relationships which may be considered as potential competing interests: Shahab Mirjalili reports financial support was provided by Palo Alto Research Center Incorporated (grant 249996).

Data availability

Data will be made available on request.

Acknowledgements

We acknowledge financial support from Palo Alto Research Center (grant 249996).

Appendix A. Pseudo-algorithm for consistent, energy-conserving simulation of N -phase flows

A 2D setting with uniform, equal grid spacing in x and y is considered here for simplicity. The time-step must be chosen based on numerical stability and boundedness, as explained in Section 4. To clearly highlight the spatial discretizations, the pseudo-algorithm is presented for first order explicit Euler time integration. Extension to higher order time-stepping schemes is straight-forward. To simplify notation we denote the velocity in the x and y direction with u and v . The x component of velocity on the left face of the (i, j) -th cell is thus $u_{i-1/2,j}$. A similar format is used for the mass fluxes, by which U and V represent the x and y components of the mass flux, $\rho\vec{u} - \vec{S}$, respectively (see Eqs. (6)-(9)). Note that linear interpolation is used to compute quantities such as density on the face (e.g., $\rho_{i-1/2,j}^k = (\rho_{i,j}^k + \rho_{i-1,j}^k)/2$). For time step k :

1. Compute pairwise normal vectors \vec{n}_{pq} at the cell centers:

- Compute pairwise volume fractions at the cell centers: $\phi_{pq,i,j}^k = \frac{\phi_{p,i,j}^k}{\phi_{p,i,j}^k + \phi_{q,i,j}^k}$
- Compute $\nabla\phi_{pq}$ at cell centers: $\nabla\phi_{pq,i,j}^k = (\frac{\phi_{pq,i+1,j}^k - \phi_{pq,i-1,j}^k}{2\Delta x}, \frac{\phi_{pq,i,j+1}^k - \phi_{pq,i,j-1}^k}{2\Delta y})$
- Compute $\vec{n}_{pq,i,j}^k = \frac{\nabla\phi_{pq,i,j}^k}{|\nabla\phi_{pq,i,j}^k|}$ at the cell centers

2. Compute density and viscosity at the cell centers:

- $\rho_{i,j}^k = \sum_{p=1}^N \rho_p \phi_{p,i,j}^k$
- $\mu_{i,j}^k = \sum_{p=1}^N \mu_p \phi_{p,i,j}^k$

3. Compute velocity (momentum per unit mass):

$$u_{i-1/2,j}^k = \frac{(\rho u)_{i-1/2,j}^k}{\rho_{i-1/2,j}^k}$$

$$v_{i,j-1/2}^k = \frac{(\rho v)_{i,j-1/2}^k}{\rho_{i,j-1/2}^k}$$

4. Compute body forces (including surface tension forces):

- Compute curvature at cell centers:

$$\kappa_{pq,i,j}^k = -\nabla \cdot \vec{n}_{pq,i,j}^k = -(\frac{n_{pq,x,i+1,j}^k - n_{pq,x,i-1,j}^k}{2\Delta x} + \frac{n_{pq,y,i,j+1}^k - n_{pq,y,i,j-1}^k}{2\Delta y})$$

- Compute the surface tension forces on the faces:

$$f_{x,i-1/2,j}^k = \sum_{p < q} 6\sigma_{pq} \phi_{p,i,j}^k \phi_{q,i,j}^k \frac{\kappa_{pq,i,j}^k + \kappa_{pq,i-1,j}^k}{2} \frac{\phi_{pq,i,j}^k - \phi_{pq,i-1,j}^k}{\Delta x}$$

$$f_{y,i,j-1/2}^k = \sum_{p < q} 6\sigma_{pq} \phi_{p,i,j}^k \phi_{q,i,j}^k \frac{\kappa_{pq,i,j}^k + \kappa_{pq,i,j-1}^k}{2} \frac{\phi_{pq,i,j}^k - \phi_{pq,i,j-1}^k}{\Delta y}$$

5. Compute viscous stresses, $\tau_{xx,i,j}^k$, $\tau_{xy,i-1/2,j-1/2}^k$, $\tau_{yy,i,j}^k$ and $\tau_{yx,i-1/2,j-1/2}^k$ using $\mu_{i,j}^k$, $u_{i-1/2,j}^k$ and $v_{i,j-1/2}^k$ fields. Standard linear interpolation operators are used for computing $\mu_{i-1/2,j-1/2}^k$ values.

6. Compute ϕ_p values ($1 \leq p \leq N - 1$) at time step $k + 1$:

- Compute the sharpening fluxes at the cell centers:

$$\tilde{s}_{p,i,j}^k = -\sum_{q \neq p} \frac{\phi_{p,i,j}^k \phi_{q,i,j}^k}{(\epsilon_{pq}/\ell)} \vec{n}_{pq,i,j}^k$$

- Compute the RHS phase field fluxes on the mesh faces:

$$a_{p,x,i-1/2,j}^k = \gamma(\frac{s_{p,x,i,j}^k + s_{p,x,i-1,j}^k}{2} + \epsilon \frac{\phi_{p,i,j}^k - \phi_{p,i-1,j}^k}{\Delta x})$$

$$a_{p,y,i,j-1/2}^k = \gamma(\frac{s_{p,y,i,j}^k + s_{p,y,i,j-1}^k}{2} + \epsilon \frac{\phi_{p,i,j}^k - \phi_{p,i,j-1}^k}{\Delta y})$$

- Compute

$$\phi_{p,i,j}^{k+1} = \phi_{p,i,j}^k + (\Delta t)[\frac{(-u_{i+1/2,j}^k \phi_{p,i+1/2,j}^k + a_{p,x,i+1/2,j}^k) - (-u_{i-1/2,j}^k \phi_{p,i-1/2,j}^k + a_{p,x,i-1/2,j}^k)}{\Delta x} + \frac{(-v_{i,j+1/2}^k \phi_{p,i,j+1/2}^k + a_{p,y,i,j+1/2}^k) - (-v_{i,j-1/2}^k \phi_{p,i,j-1/2}^k + a_{p,y,i,j-1/2}^k)}{\Delta y}]$$

- Compute ϕ_N using volume conservation: $\phi_{N,i,j}^{k+1} = 1 - \sum_{p=1}^{N-1} \phi_{p,i,j}^{k+1}$

7. Compute the mass fluxes on the faces. This mass flux must be used for transport of any transporter that is defined on a per-unit mass basis. This includes momentum per unit mass, or velocity:

$$U_{i-1/2,j}^k = (\rho u)_{i-1/2,j}^k - \sum_{p=1}^N \rho_p a_{p,x,i-1/2,j}^k$$

$$V_{i,j-1/2}^k = (\rho v)_{i,j-1/2}^k - \sum_{p=1}^N \rho_p a_{p,y,i,j-1/2}^k$$

8. Compute the density values at cell centers at time-step $k + 1$:

$$\rho_{i,j}^{k+1} = \sum_{p=1}^N \rho_p \phi_{p,i,j}^{k+1}$$

9. Compute intermediate values for ρu and ρv . This is also known as the predictor step:

$$\begin{aligned} (\rho u)_{i-1/2,j}^* &= (\rho u)_{i-1/2,j}^k - (\Delta t) \left(\frac{\frac{U_{i+1/2,j}^k + U_{i-1/2,j}^k}{2} \frac{u_{i+1/2,j}^k + u_{i-1/2,j}^k}{2} - \frac{U_{i-1/2,j}^k + U_{i-3/2,j}^k}{2} \frac{u_{i-1/2,j}^k + u_{i-3/2,j}^k}{2}}{\Delta x} \right. \\ &\quad \left. + \frac{V_{i-1/2,j+1/2}^k \frac{u_{i-1/2,j+1}^k + u_{i-1/2,j}^k}{2} - V_{i-1/2,j-1/2}^k \frac{u_{i-1/2,j+1}^k + u_{i-1/2,j-1}^k}{2}}{\Delta y} \right) + \frac{P_{i,j}^k - P_{i-1,j}^k}{\Delta x} - \frac{\tau_{xx,i,j}^k - \tau_{xx,i-1,j}^k}{\Delta x} - \\ &\quad \frac{\tau_{xy,i-1/2,j+1/2}^k - \tau_{xy,i-1/2,j-1/2}^k}{\Delta y} - f_{x,i-1/2,j}^k \Big) \\ (\rho v)_{i,j-1/2}^* &= (\rho v)_{i,j-1/2}^k - (\Delta t) \left(\frac{\frac{U_{i+1/2,j-1/2}^k + U_{i-1/2,j-1/2}^k}{2} \frac{v_{i+1/2,j-1/2}^k + v_{i-1/2,j-1/2}^k}{2} - \frac{U_{i-1/2,j-1/2}^k + U_{i-3/2,j-1/2}^k}{2} \frac{v_{i-1/2,j-1/2}^k + v_{i-3/2,j-1/2}^k}{2}}{\Delta x} \right. \\ &\quad \left. + \frac{V_{i,j+1/2}^k + V_{i,j-1/2}^k}{2} \frac{v_{i,j+1/2}^k + v_{i,j-1/2}^k}{2} - \frac{V_{i,j-1/2}^k + V_{i,j-3/2}^k}{2} \frac{v_{i,j-1/2}^k + v_{i,j-3/2}^k}{2} \right) + \frac{P_{i,j}^k - P_{i,j-1}^k}{\Delta y} - \frac{\tau_{yy,i,j}^k - \tau_{yy,i,j-1}^k}{\Delta y} - \\ &\quad \frac{\tau_{yx,i+1/2,j-1/2}^k - \tau_{yx,i-1/2,j-1/2}^k}{\Delta x} - f_{y,i,j-1/2}^k \Big) \end{aligned}$$

10. Compute the pressure correction that would enforce a solenoidal velocity field ($\frac{u_{i+1/2,j}^{k+1} - u_{i-1/2,j}^{k+1}}{\Delta x} + \frac{v_{i,j+1/2}^{k+1} - v_{i,j-1/2}^{k+1}}{\Delta y} = 0$):

- Compute RHS of Poisson system at the cell center:

$$(RHS)_{i,j}^k = (1/\Delta t) \left(\frac{\frac{(\rho u)_{i+1/2,j}^* - (\rho u)_{i-1/2,j}^*}{\Delta x}}{\rho_{i+1/2,j}^{k+1}} + \frac{\frac{(\rho v)_{i,j+1/2}^* - (\rho v)_{i,j-1/2}^*}{\Delta y}}{\rho_{i,j+1/2}^{k+1}} \right)$$

- Solve Poisson system to find $\delta P_{i,j} = P_{i,j}^{k+1} - P_{i,j}^k$:

$$\frac{\frac{\delta P_{i+1,j} - \delta P_{i,j}}{\rho_{i+1/2,j}^{k+1} \Delta x} - \frac{\delta P_{i,j} - \delta P_{i-1,j}}{\rho_{i-1/2,j}^{k+1} \Delta x}}{\Delta x} + \frac{\frac{\delta P_{i,j+1} - \delta P_{i,j}}{\rho_{i,j+1/2}^{k+1} \Delta y} - \frac{\delta P_{i,j} - \delta P_{i,j-1}}{\rho_{i,j-1/2}^{k+1} \Delta y}}{\Delta y} = (RHS)_{i,j}^k$$

11. The corrector step:

- Update the value of pressure at time-step $k + 1$:

$$P_{i,j}^{k+1} = P_{i,j}^k + \delta P_{i,j}$$

- Compute the values of ρu and ρv at time-step $k + 1$:

$$(\rho u)_{i-1/2,j}^{k+1} = (\rho u)_{i-1/2,j}^* - \Delta t \left(\frac{\delta P_{i,j} - \delta P_{i-1,j}}{\Delta x} \right)$$

$$(\rho v)_{i,j-1/2}^{k+1} = (\rho v)_{i,j-1/2}^* - \Delta t \left(\frac{\delta P_{i,j} - \delta P_{i,j-1}}{\Delta y} \right)$$

12. Advance time $t = t + \Delta t$, return to step 1 with $k = k + 1$

References

- [1] P.-H. Chiu, Y.-T. Lin, A conservative phase field method for solving incompressible two-phase flows, *J. Comput. Phys.* 230 (1) (2011) 185–204.
- [2] J. Beyer, H.C. Trannum, T. Bakke, P.V. Hodson, T.K. Collier, Environmental effects of the deepwater horizon oil spill: a review, *Mar. Pollut. Bull.* 110 (1) (2016) 28–51.
- [3] V. Alvarado, E. Manrique, Enhanced oil recovery: an update review, *Energies* 3 (9) (2010) 1529–1575.
- [4] A. Maghzi, S. Mohammadi, M.H. Ghazanfari, R. Kharrat, M. Masihi, Monitoring wettability alteration by silica nanoparticles during water flooding to heavy oils in five-spot systems: a pore-level investigation, *Exp. Therm. Fluid Sci.* 40 (2012) 168–176.
- [5] H. Li, Y. Tang, Z. Wang, Z. Shi, S. Wu, D. Song, J. Zhang, K. Fatih, J. Zhang, H. Wang, et al., A review of water flooding issues in the proton exchange membrane fuel cell, *J. Power Sources* 178 (1) (2008) 103–117.
- [6] A.S. Utada, E. Lorenceau, D.R. Link, P.D. Kaplan, H.A. Stone, D. Weitz, Monodisperse double emulsions generated from a microcapillary device, *Science* 308 (5721) (2005) 537–541.
- [7] A. Tiribocchi, A. Montessori, M. Lauricella, F. Bonaccorso, S. Succi, S. Aime, M. Milani, D. Weitz, The vortex-driven dynamics of droplets within droplets, *Nat. Commun.* 12 (1) (2021) 1–10.
- [8] R. Seemann, M. Brinkmann, T. Pfohl, S. Herminghaus, Droplet based microfluidics, *Rep. Prog. Phys.* 75 (1) (2011) 016601.
- [9] S. Korneev, Z. Wang, V. Thiagarajan, S. Nelaturi, Fabricated shape estimation for additive manufacturing processes with uncertainty, *Comput. Aided Des.* 127 (2020) 102852.
- [10] A. Prosperetti, G. Tryggvason, *Computational Methods for Multiphase Flow*, Cambridge University Press, 2009.
- [11] G. Tryggvason, R. Scardovelli, S. Zaleski, *Direct Numerical Simulations of Gas–Liquid Multiphase Flows*, Cambridge University Press, 2011.
- [12] S. Mirjalili, S.S. Jain, M. Dodd, *Interface-Capturing Methods for Two-Phase Flows: An Overview and Recent Developments*, Center for Turbulence Research Annual Research Briefs, 2017, pp. 117–135.
- [13] S.P. Schofield, R.V. Garimella, M.M. Francois, R. Loubère, A second-order accurate material-order-independent interface reconstruction technique for multi-material flow simulations, *J. Comput. Phys.* 228 (3) (2009) 731–745.
- [14] B. Blais, J.-P. Braeunig, D. Chauveheid, J.-M. Ghidaglia, R. Loubère, Dealing with more than two materials in the fvcf-enip method, *Eur. J. Mech. B, Fluids* 42 (2013) 1–9.
- [15] A. Pathak, M. Raessi, A three-dimensional volume-of-fluid method for reconstructing and advecting three-material interfaces forming contact lines, *J. Comput. Phys.* 307 (2016) 550–573.
- [16] A.K. Pandare, J. Waltz, J. Bakosi, Multi-material hydrodynamics with algebraic sharp interface capturing, *Comput. Fluids* 215 (2021) 104804.
- [17] F. Losasso, T. Shinar, A. Selle, R. Fedkiw, Multiple interacting liquids, *ACM Trans. Graph.* 25 (3) (2006) 812–819.
- [18] D.P. Starinshak, S. Karni, P.L. Roe, A new level set model for multimaterial flows, *J. Comput. Phys.* 262 (2014) 1–16.
- [19] H. Li, Y. Yap, J. Lou, Z. Shang, Numerical modelling of three-fluid flow using the level-set method, *Chem. Eng. Sci.* 126 (2015) 224–236.
- [20] A.A. Howard, A.M. Tartakovsky, A conservative level set method for n-phase flows with a free-energy-based surface tension model, *J. Comput. Phys.* 426 (2021) 109955.
- [21] J. Kim, A generalized continuous surface tension force formulation for phase-field models for multi-component immiscible fluid flows, *Comput. Methods Appl. Mech. Eng.* 198 (37–40) (2009) 3105–3112.

- [22] F. Boyer, C. Lapuerta, S. Minjeaud, B. Piar, M. Quintard, Cahn–Hilliard/Navier–Stokes model for the simulation of three-phase flows, *Transp. Porous Media* 82 (3) (2010) 463–483.
- [23] J. Kim, Phase-field models for multi-component fluid flows, *Commun. Comput. Phys.* 12 (3) (2012) 613–661.
- [24] S. Dong, An efficient algorithm for incompressible n-phase flows, *J. Comput. Phys.* 276 (2014) 691–728.
- [25] S. Wu, J. Xu, Multiphase Allen–Cahn and Cahn–Hilliard models and their discretizations with the effect of pairwise surface tensions, *J. Comput. Phys.* 343 (2017) 10–32.
- [26] J. Kim, H.G. Lee, A new conservative vector-valued Allen–Cahn equation and its fast numerical method, *Comput. Phys. Commun.* 221 (2017) 102–108.
- [27] S. Dong, Multiphase flows of n immiscible incompressible fluids: a reduction-consistent and thermodynamically-consistent formulation and associated algorithm, *J. Comput. Phys.* 361 (2018) 1–49.
- [28] S. Aihara, T. Takaki, N. Takada, Multi-phase-field modeling using a conservative Allen–Cahn equation for multiphase flow, *Comput. Fluids* 178 (2019) 141–151.
- [29] M. Adler, S. Jain, J. West, A. Mani, S. Lele, Diffuse Interface Capturing Methods for Compressible Multiphase Fluid Flows and Elasticplastic Deformation in Solids: Part I. Methods, Annual Research Briefs, Center for Turbulence Research, Stanford University, 2020, pp. 341–356.
- [30] Z. Huang, G. Lin, A.M. Ardekani, A consistent and conservative model and its scheme for n-phase-m-component incompressible flows, *J. Comput. Phys.* 434 (2021) 110229.
- [31] H. Liang, B. Shi, Z. Chai, Lattice Boltzmann modeling of three-phase incompressible flows, *Phys. Rev. E* 93 (1) (2016) 013308.
- [32] R.H.H. Abadi, A. Fakhari, M.H. Rahimian, Numerical simulation of three-component multiphase flows at high density and viscosity ratios using lattice Boltzmann methods, *Phys. Rev. E* 97 (3) (2018) 033312.
- [33] R.H.H. Abadi, M.H. Rahimian, A. Fakhari, Conservative phase-field lattice-Boltzmann model for ternary fluids, *J. Comput. Phys.* 374 (2018) 668–691.
- [34] Q. He, Y. Li, W. Huang, Y. Hu, D. Li, Y. Wang, A unified lattice Boltzmann model for immiscible and miscible ternary fluids, *Comput. Math. Appl.* 80 (12) (2020) 2830–2859.
- [35] L. Zheng, S. Zheng, Q. Zhai, Reduction-consistent phase-field lattice Boltzmann equation for n immiscible incompressible fluids, *Phys. Rev. E* 101 (4) (2020) 043302.
- [36] Y. Hu, D. Li, Q. He, Generalized conservative phase field model and its lattice Boltzmann scheme for multicomponent multiphase flows, *Int. J. Multiph. Flow* 132 (2020) 103432.
- [37] L. Zheng, S. Zheng, Q. Zhai, Reduction-consistent Cahn–Hilliard theory based lattice Boltzmann equation method for n immiscible incompressible fluids, *Phys. A, Stat. Mech. Appl.* 574 (2021) 126015.
- [38] X. Yuan, B. Shi, C. Zhan, Z. Chai, A phase-field-based lattice Boltzmann model for multiphase flows involving n immiscible incompressible fluids, *Phys. Fluids* 34 (2) (2022) 023311.
- [39] S.-T. Zhang, J.-X. Zhou, H.-W. Xiao, X.-D. Niu, H. Wei, A. Khan, D.-C. Li, H. Yamaguchi, A generalized conservative phase-field simplified lattice Boltzmann method for miscible and immiscible ternary flows with large density ratio, *Int. J. Multiph. Flow* (2022) 103978.
- [40] D. Anderson, G. McFadden, A. Wheeler, Diffuse-interface methods in fluid mechanics, *Annu. Rev. Fluid Mech.* 30 (1998) 139–165.
- [41] S. Mirjalili, C.B. Ivey, A. Mani, Comparison between the diffuse interface and volume of fluid methods for simulating two-phase flows, *Int. J. Multiph. Flow* 116 (2019) 221–238.
- [42] P. Yue, C. Zhou, J.J. Feng, Spontaneous shrinkage of drops and mass conservation in phase-field simulations, *J. Comput. Phys.* 223 (2007) 1–9.
- [43] S. Dai, Q. Du, Computational studies of coarsening rates for the Cahn–Hilliard equation with phase-dependent diffusion mobility, *J. Comput. Phys.* 310 (2016) 85–108.
- [44] G. Soligo, A. Roccon, A. Soldati, Mass-conservation-improved phase field methods for turbulent multiphase flow simulation, *Acta Mech.* 230 (2) (2019) 683–696.
- [45] G. Fu, D. Han, A linear second-order in time unconditionally energy stable finite element scheme for a Cahn–Hilliard phase-field model for two-phase incompressible flow of variable densities, *Comput. Methods Appl. Math.* 387 (2021) 114186.
- [46] M.A. Khanwale, K. Saurabh, M. Ishii, H. Sundar, B. Ganapathysubramanian, Breakup dynamics in primary jet atomization using mesh-and interface-refined Cahn–Hilliard Navier–Stokes, 2022, arXiv:2209.13142.
- [47] J. Kim, S. Lee, Y. Choi, A conservative Allen–Cahn equation with a space-time dependent Lagrange multiplier, *Int. J. Eng. Sci.* 84 (2014) 11–17.
- [48] S. Zhai, Z. Weng, X. Feng, Investigations on several numerical methods for the non-local Allen–Cahn equation, *Int. J. Heat Mass Transf.* 87 (2015) 111–118.
- [49] D. Jeong, J. Kim, Conservative Allen–Cahn–Navier–Stokes system for incompressible two-phase fluid flows, *Comput. Fluids* 156 (2017) 239–246.
- [50] V. Joshi, R.K. Jaiman, A positivity preserving and conservative variational scheme for phase-field modeling of two-phase flows, *J. Comput. Phys.* 360 (2018) 137–166.
- [51] Z. Huang, G. Lin, A.M. Ardekani, Consistent and conservative scheme for incompressible two-phase flows using the conservative Allen–Cahn model, *J. Comput. Phys.* 420 (2020) 109718.
- [52] S. Mirjalili, C.B. Ivey, A. Mani, A conservative diffuse interface method for two-phase flows with provable boundedness properties, *J. Comput. Phys.* 401 (2020) 109006.
- [53] S. Mirjalili, A. Mani, Consistent, energy-conserving momentum transport for simulations of two-phase flows using the phase field equations, *J. Comput. Phys.* 426 (2021) 109918.
- [54] S. Mirjalili, M.A. Khanwale, A. Mani, Assessment of an energy-based surface tension model for simulation of two-phase flows using second-order phase field methods, *J. Comput. Phys.* 474 (2023) 111795.
- [55] L. Zheng, S. Zheng, Q. Zhai, Multiphase flows of n immiscible incompressible fluids: conservative Allen–Cahn equation and lattice Boltzmann equation method, *Phys. Rev. E* 101 (1) (2020) 013305.
- [56] C. Zhan, X. Liu, Z. Chai, B. Shi, A comparative study of two Allen–Cahn models for immiscible n-phase flows by using a consistent and conservative lattice Boltzmann method, preprint, arXiv:2306.06983.
- [57] J.D. van der Waals, The thermodynamic theory of capillarity under the hypothesis of a continuous variation of density, *J. Stat. Phys.* 20 (2) (1979) 200–244.
- [58] J.W. Cahn, J.E. Hilliard, Free energy of a nonuniform system. I. Interfacial free energy, *J. Chem. Phys.* 28 (2) (1958) 258–267.
- [59] S.M. Allen, J.W. Cahn, A microscopic theory for antiphase boundary motion and its application to antiphase domain coarsening, *Acta Metall.* 27 (6) (1979) 1085–1095.
- [60] P.-G. De Gennes, F. Brochard-Wyart, D. Quéré, et al., *Capillarity and Wetting Phenomena: Drops, Bubbles, Pearls, Waves*, vol. 315, Springer, 2004.
- [61] P. Moin, *Fundamentals of Engineering Numerical Analysis*, Cambridge University Press, 2010.
- [62] I. Langmuir, Oil lenses on water and the nature of monomolecular expanded films, *J. Chem. Phys.* 1 (11) (1933) 756–776.
- [63] J. Zou, P.F. Wang, T.R. Zhang, X. Fu, X. Ruan, Experimental study of a drop bouncing on a liquid surface, *Phys. Fluids* 23 (4) (2011) 044101.
- [64] Z. Wu, J. Hao, J. Lu, L. Xu, G. Hu, J. Floryan, Small droplet bouncing on a deep pool, *Phys. Fluids* 32 (1) (2020) 012107.
- [65] S. Mirjalili, A. Mani, Transitional stages of thin air film entrainment in drop-pool impact events, *J. Fluid Mech.* 901 (2020) A14.